MNRAS **000**, 1–21 (2020) Preprint 28th October 2020 Compiled using MNRAS LATEX style file v3.0

Disk dominated galaxies retain their shapes below $z = 1.0$

K. Hoffmann[1]★, C. Laigle[2], N. E. Chisari[3], P. Tallada[4,5], Y. Dubois[2], J. Devriendt[6]
[1] *Institute for Computational Science, University of Zurich, Winterthurerstr. 190, 8057 Zürich, Switzerland*
[2] *CNRS and UPMC Univ. Paris 06, UMR 7095, Institut d'Astrophysique de Paris, 98 bis Boulevard Arago, F-75014 Paris, France*
[3] *Institute for Theoretical Physics, Utrecht University, Princetonplein 5, 3584 CC Utrecht, The Netherlands*
[4] *Centro de Investigaciones Energéticas, Medioambientales y Tecnológicas (CIEMAT), Avenida Complutense 40, 28040 Madrid, Spain*
[5] *Port d'Informació Científica (PIC), Campus UAB, C. Albareda s/n, 08193 Bellaterra (Barcelona), Spain*
[6] *Astrophysics, University of Oxford, Denys Wilkinson Building, Keble Road, Oxford, OX1 3RH, UK*

Accepted XXX. Received YYY; in original form ZZZ

ABSTRACT

The high abundance of disk galaxies without a large central bulge challenges predictions of current hydrodynamic simulations of galaxy formation. We aim to shed light on the formation of these objects by studying the redshift and mass dependence of their 3D shape distribution in the COSMOS galaxy survey. This distribution is inferred from the observed distribution of 2D shapes, using a reconstruction method which we test using hydrodynamic simulations. We find a moderate bias for the inferred average disk circularity and relative thickness with respect to the disk radius, but a large bias on the dispersion of these quantities. Applying the 3D shape reconstruction method on COSMOS data, we find no significant dependence of the inferred 3D shape distribution on redshift. The relative disk thickness shows a significant mass dependence which can be accounted for by the scaling of disk radius with galaxy mass. We conclude that the shapes of disk dominated galaxies are overall not subject to disruptive merging or feedback events below redshift $z = 1.0$. This favours a scenario where these disks form early and subsequently undergo a tranquil evolution in isolation. In addition, our study shows that the observed 2D shapes of disk dominated galaxies can be well fitted using an ellipsoidal model for the galaxy 3D morphology combined with a Gaussian model for the 3D axes ratio distribution, confirming findings from similar work reported in the literature. Such an approach allows to build realistic mock catalogs with intrinsic galaxy shapes that will be essential for the study of intrinsic galaxy alignment as a contaminant of weak lensing surveys.

Key words: galaxies: spiral – galaxies: evolution – galaxies: statistics – methods: statistical

1 INTRODUCTION

The structure of late-type galaxies is comprised of different components with distinct kinematic and morphological characteristics. The most prominent of these components is the thin stellar disk with its spiral arm over densities. Observations at low redshifts and in our own Milky Way revealed that this thin disk is often enclosed by a thick stellar disk as well as a stellar halo with relatively low densities (e.g. Carollo et al. 2010; Trujillo & Bakos 2013; Martínez-Lombilla & Knapen 2019, among others). Near the galactic center, the spiral arms of most disks transition either into a bar or into a bulge. The contribution of these components to the overall mass and morphology of a given galaxy is determined by the galaxies' formation history (e.g. Binney & Tremaine 2008; Vogelsberger et al. 2020). Therefore, studying how the shapes of late-type galaxies (hereafter referred to as disk galaxies) are distributed at different epochs of the Universe can provide significant insights into the processes which dominate galaxy formation, as detailed below.

During the recent years it was pointed out that the observed abundance of a particular type of objects, namely disk dominated galaxies with only a small or no central bulge, challenges our current understanding of galaxy formation in ΛCDM (e.g. Kormendy et al. 2010). As a matter of fact, bulges are expected to form in galaxies for several reasons. van den Bosch (1998) suggested that bulges can form "inside out" from the low angular momentum components of the initial gas overdensities in which the galaxies are born (see also Kepner 1999). In another popular scenario, bulges result from the redistribution of angular momentum within the disk by central bars, spiral arms or bending instabilities which distort the stellar orbits (Kormendy & Kennicutt 2004; Debattista et al. 2006). This so-called "secular evolution" leads typically to the formation of a small "pseudo" bulge, but may also promote the emergence of a larger classical bulge when occurring at high redshifts (Elmegreen et al. 2008; Bournaud 2016). A third and important scenario for bulge formation is the accretion of satellite galaxies, globular clusters or streams of cold gas, which can move low angular momentum material to the center of the disk (e.g. through violent disk instabilities) without destroying it (e.g. Hopkins et al. 2009; Walker et al. 1996;

★ E-mail: hoffmann@ics.uzh.ch

Dubois et al. 2012; Kretschmer et al. 2020). Since mergers and cold flows are believed to play a significant role in the formation and growth of disk galaxies (e.g. Baugh et al. 1996; Kauffmann et al. 1993; Aguerri et al. 2001; Eliche-Moral et al. 2006) it is difficult to explain how a significant fraction of high mass disks (i.e. $M_\star \gtrsim 10^{10} M_\odot$) could grow without forming a large bulge (Kautsch et al. 2006; Kautsch 2009; Weinzirl et al. 2009; Buta et al. 2015).

One possible solution to this unsolved problem are feedback processes which can suppress the formation of a bulge by removing low angular momentum material from the disk, in particular after gas-rich major mergers (e.g. Governato et al. 2010; Brook et al. 2011, 2012; Hopkins et al. 2012; Übler et al. 2014; Dubois et al. 2016; Grand et al. 2017). However, simulations suggest that this suppression is only effective for disks with stellar masses of the Milky Way ($\simeq 6 \times 10^{10} \mathrm{M}_\odot$) or below, but not at higher masses (Brooks & Christensen 2016). An additional challenge for formation scenarios including major mergers are the low density environments in which bulgeless disks typically reside (e.g. Grossi et al. 2018). Kormendy et al. (2010); Kormendy (2016) argue that this finding speaks for for a gentle, rather than violent mass accretion history. Recently, Peebles (2020) therefore discussed an alternative solution to the problem, according to which small scale non-Gaussianities in the initial conditions of a warm or mixed dark matter universe could lead to a large fraction of bulge-less disks. However, this approach remains to be explored with simulations of galaxy formation.

In this work we aim to shed light on the formation of bulge-less disks, using a novel approach for discriminating the first scenario in which feedback processes suppress bulge formation after mergers from alternative, less violent mass accretion scenarios by studying the shape evolution of observed disk dominated galaxies. We thereby rely on the hypothesis that disruptive events, such as mergers and strong feedback should dramatically affect the morphology of the remaining galactic disk, besides the absence of bulge. One would therefore expect a significant mass and redshift dependence of the disks thickness and circularity. On the contrary, if the bulge-less disks underwent an early and regular accretion of mass, for instance through infalling cold streams at high redshifts followed by a calm evolution without major mergers, their morphologies should exhibit little or no dependency on mass and redshift.

A challenging aspect of this endeavour is to interpret the observed two-dimensional (2D) galaxy shapes in terms of 3D models of galaxy formation. One way of establishing such an interpretation is the forward modeling of the observed 2D shapes based on galaxies from hydrodynamic simulations in cosmological volumes. It has been shown that mock galaxy images constructed from the simulations Illustris TNG and EAGLE have similar morphological properties as low redshift observations from GAMA and Pan-STARRS (e.g. Rodriguez-Gomez et al. 2019; Bignone et al. 2020). However, drawing detailed conclusions from such a comparison is hampered by the fact that the simulations parameter space cannot be explored due to the high computational costs required for the production and post-processing. In addition such large hydrodynamical simulations inevitably have to compromise between volume and resolution, and their predictive power regarding galaxy shapes is limited to the regime where these galaxies are sufficiently well resolved.

We therefore follow an alternative approach for interpreting the observed 2D galaxy shape distribution, based on a simplistic ellipsoidal model for the 3D light distribution within a given galaxy. The shape of the ellipsoids is thereby fully characterized by two of the three possible ratios between the major, intermediate and minor axes (A_{3D}, B_{3D} and C_{3D} respectively),

$$q_{3D} \equiv \frac{B_{3D}}{A_{3D}}, \quad r_{3D} \equiv \frac{C_{3D}}{B_{3D}}, \quad s_{3D} \equiv \frac{C_{3D}}{A_{3D}}. \tag{1}$$

For disk galaxies the q_{3D} parameter can be regarded as a measure for the circularity, while r_{3D} and s_{3D} quantify the relative disk thickness. The 2D galaxy shapes of the projected ellipsoid are described by the axes ratio

$$q_{2D} \equiv \frac{B_{2D}}{A_{2D}}. \tag{2}$$

The main advantage of such an ellipsoidal approximation is that the distribution of 2D axes ratios can be predicted from a given model for the 3D axes ratio distribution at low computational cost. This allows for the reconstruction of the 3D axes ratio distribution by tuning the corresponding model parameters such that the predicted distribution of 2D axes ratios matches observations. This reconstruction technique dates back to Hubble (1926) who derived first constraints on the intrinsic 3D axes ratios of galaxies by modeling them as oblate ellipsoids. Over the last century it has been shown that, despite its simplicity, this methodology reproduces the observed 2D axes ratio distribution of late as well as of early type galaxies, assuming oblate or prolate ellipsoidal models (e.g. Sandage et al. 1970; Binney 1978; Noerdlinger 1979). The agreement with observed axes ratio distributions was further improved by modeling galaxies as triaxial ellipsoids, which allowed for more detailed interpretations of the observations (Benacchio & Galletta 1980; Binney & de Vaucouleurs 1981; Lambas et al. 1992). These early studies where continued using larger samples to study the relation between intrinsic galaxy shapes and properties, such as size, luminosity, color in the local universe, observed by the Sloan Digital Sky surveys (e.g. Ryden 2004; Vincent & Ryden 2005; Padilla & Strauss 2008; Rodríguez & Padilla 2013). The evolution of intrinsic shapes with redshift has been studied in galaxy surveys such as SDSS, 3D-HST, GOODS, COSMOS and CANDELS (Yuma et al. 2011, 2012; Holden et al. 2012; Chang et al. 2013; van der Wel et al. 2014; Takeuchi et al. 2015; Zhang et al. 2019; Satoh et al. 2019). Physical interpretations drawn from these reconstructed axes ratio distributions rely on the validity of the ellipsoidal model for the 3D galaxy shapes as well as on the accuracy of the model for the 3D axes ratio distribution. In addition, observational sources of systematics on the observed 2D axes ratio distribution, for example those induced by dust extinction within the galaxy, need to be taken into account in the analysis.

The objective of our analysis is therefore two fold. Our main goal is to constrain potential explanations for the absence of large bulges in disk galaxies based on the reconstructed 3D shape distribution of disk dominated galaxies as outlined earlier in this section. Our investigation is based on data from the COSMOS galaxy survey (Scoville et al. 2007), which provides excellent imaging of galaxies over a wide range of redshifts and stellar masses, and is therefore ideal for our analysis. However, strong uncertainties can be expected from our simplistic assumptions used in the reconstruction of the 3D shape distribution. Our second goal is therefore to test several of these assumptions as well as the overall performance of the reconstruction method using the state-of-the-art hydrodynamic simulations of galaxy formation Horizon AGN and Illustris TNG.

This paper is structured as follows. In Section 2, we present the galaxy catalogues from the COSMOS survey and the hydrodynamic simulations and explain our sample selection. Section 3 provides details on the shape reconstruction method together with validations of the model assumptions and accuracy tests. The method is then applied on the COSMOS data in Section 4. A summary of our results can be found together with our conclusions in Section 5.

2 DATA

2.1 COSMOS observations

The 2 deg^2 COSMOS field (Scoville et al. 2007) has been observed extensively by different ground and space based telescopes, including Hubble, Spitzer, VISTA, CFHT and Subaru. The joint analysis of these observations led to different catalogs providing estimates of galaxy properties, stellar masses, star formation rates and morphological characteristics over a large range in redshift and luminosity. Our analysis is based on three of these catalogs, which are described below.

2.1.1 *Photometry*

The public COSMOS2015 catalogue [1] (Laigle et al. 2016) comprises photometry in 30 bands, covering ultra-violet to mid-infrared wavelengths. In our analysis we use redshift, stellar mass and specific star formation rate (sSFR)[2] estimates provided in this catalogue, which were derived for each galaxy by fitting templates of spectral energy distributions (SEDs) to the photometric data (Ilbert et al. 2006). We discard objects which are i) residing in regions flagged as "bad" (mostly because they are close to stars or to the edge of the field) ii) saturated and iii) not classified as galaxies by requiring the corresponding catalogue flags to be `[flag_hjmcc, flag_peter, type] = [0,0,0]`. We further impose cuts at the limiting AB magnitudes in the near-infrared K_s-band of 24.0 and 24.7 in the *deep* and ultra *ultra-deep* fields respectively. These magnitudes are defined within a fixed 3″ diameter aperture (`Ks_MAG_APER3`) and the limits correspond to a 3σ detection. After applying these cuts the catalogue contains 252, 527 galaxies. For this sample the standard deviation of the relative differences in redshift with respect to the zCOSMOS-bright spectroscopic control sample (Lilly et al. 2007) is $\sigma_{\Delta z/(1+z_s)} = 0.007$ (catastrophic failure fraction $\eta = 0.5\%$). Note that this error is an optimistic estimate, since it was inferred by comparison to spectroscopic redshifts of bright galaxies and is higher for dimmer objects. However, due to the bright magnitude cuts used in this work (see Section 2.1.5) we expect this inaccuracy to be a realistic estimate for the galaxies in our samples. The accuracy on the stellar mass and star formation rate estimates is expected to be ~ 0.1 dex and $\sim 0.2 - 0.6$ dex respectively at $z < 1.5$ (Laigle et al. 2019). These values may be lower for our samples as we focus on bright objects only. Nevertheless, Laigle et al. (2019) find evidence that the strong scatter (and bimodality) in the SFR estimates is mainly driven by the inaccurate modelling of dust extinction within the galaxies at the SED-fitting stage (see their Figure B3). We also find strong evidence of dust extinction in the galaxies from our sample (e.g. Fig. B1). We therefore study the sSFR only for disks with high apparent axes ratios, which we consider to be inclined towards a face-on orientation at which the impact of dust extinction (and dust extinction modelling) is expected to be minimal.

2.1.2 *Shapes*

We use galaxy shape estimates from the public *Advanced Camera for Surveys General Catalog* (ACS-GC [3], Griffith et al. 2012). This catalogue is based on *Hubble Space Telescope* (HST) imaging in the optical red I_{AB} broad band filter F814W. The absence of atmospheric distortions allows for an excellent image resolution, which is mainly limited by the width of the HST point spread function (PSF) of 0.085" in the F814W filter and the pixel scale of 0.03". Sources were detected using the Galapagos software (Häußler et al. 2011), which runs SExtractor (Bertin & Arnouts 1996) and Galfit (Peng et al. 2002) in two subsequent steps. Galaxy shapes are described by the two-dimensional major over minor axes ratios q_{2D}, which are derived by Galfit from fits of a single Sérsic model to each objects image. The surface brightness in this model is given by

$$\Sigma(r) = \Sigma_e \; exp\left\{-\kappa_n \left(\left(\frac{r}{r_e}\right)^{1/n} - 1\right)\right\}, \tag{3}$$

where Σ_e is the surface brightness at the effective radius r_e and the parameter κ_n is chosen such that r_e encloses half of the total flux. The Sérsic index n quantifies the concentration of the surface brightness profile. The 2D axes ratio q_{2D} enters equation (3) via $r = \sqrt{x^2 + (y/q_{2D})^2}$, where x and y are the coordinates on the major and minor axes respectively. The modeled surface brightness profiles are convolved with the ACS PSF before being compared to the reference observation during the fit. The morphological parameters from Galfit hence describe the intrinsic galaxy shapes and do not require further PSF correction. We select objects from the catalog which were classified by SExtractor as galaxies (`CLASS_STAR_HI < 0.1`) and with good fits to the Galfit model (`FLAG_GALFIT_HI=0` and `CHI2NU_HI < 2`). From the remaining sample we reject 65 objects which have axes ratios equal to zero or larger than unity or effective radii from Galfit above 750 ACS pixels (22.5″). After these cuts the final catalog contains 128, 365 objects.

2.1.3 *Morphological classification*

The *Zurich Structure & Morphology Catalog* catalogue[4] (hereafter referred to as ZEST catalogue) is derived from the same HST imaging as the ACS-GC. This catalogue provides a morphological classification for each galaxy, derived with the *Zurich Estimator of Structural Type* (ZEST). This classification is based on a principal component analysis of five non-parametric diagnostics: asymmetry, concentration, Gini coefficient, 2nd-order moment of the brightest 20% of galaxy pixels and ellipticity (Scarlata et al. 2006, 2007; Sargent et al. 2007). The catalogue contains galaxies in the COSMOS field brighter than $I_{AB} = 24$. We select objects, which i) are classified as galaxies (`[acs_mu_class, stellarity]==[1,0]`), ii) do not reside in automatically or manually masked regions (`[acs_mask, acs_masked]==[0,1]`) and iii) are not flagged as unusable or spurious (`[acs_clean, junkflag]=[1,0]`). After applying these conditions the remaining sample contains 108, 800 galaxies. The morphological classification is considered to be unreliable for galaxies with half-light radii smaller than twice the size

[1] https://www.eso.org/qi/
[2] We are aware that this sSFR estimates is not very robust, but we checked that it is sufficient for the purpose of our analysis.
[3] vizier.u-strasbg.fr/viz-bin/VizieR-3?-source=J/ApJS/200/9/acs-gc
[4] irsa.ipac.caltech.edu/data/COSMOS/tables/morphology/cosmos_morph_zurich_1.0.tbl

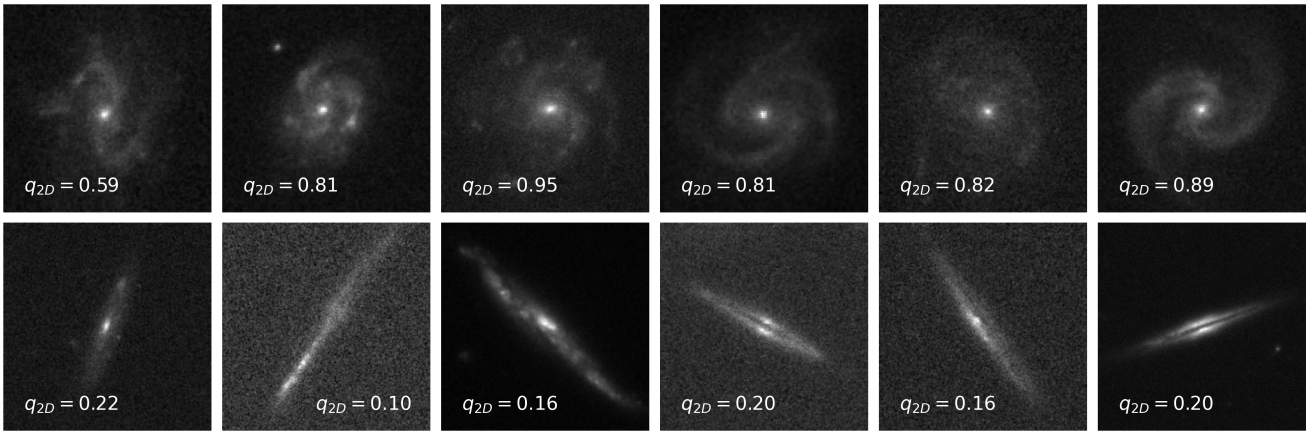

Figure 1. Examples of ACS images of late type galaxies in our volume limited COSMOS sample in the redshift range $0.2 < z < 0.4$ with face-on and edge-on orientations (top and bottom panels respectively). The galaxies are selected to be disk-dominated according to the ZEST morphological classification scheme (Section 2.1.3). The 2D axes ratios q_{2D}, provided in the ACS-GC catalogue, where obtained from single Sérsic profile fits (Section 2.1.2). The image sizes are adjusted for each galaxy.

of the ACS F814W PSF (i.e. 0.17″), which we take into account in our sample selection (Section 2.1.5).

2.1.4 *Matched catalogue*

Matching objects in these three COSMOS catalogs is not straightforward due to variations in common properties such as positions and magnitudes, which can lead to spurious mismatches. These variations can originate from atmospheric distortions in the ground-based COSMOS2015 data, differences in the employed image analysis software (i.e. SExtractor and Galfit) and its configuration, in the employed telescopes, cameras and filters, as well as different quality cuts applied before matching. In order to minimise the chance for mismatches, galaxies are matched based on angular positions as well as on magnitudes. We start by matching objects in the COSMOS2015 and ACS-GC catalog in three steps. 1) We select pairs of galaxies as candidate matches if their angular separation is $< 0.6''$, which is slightly below the typical seeing of the ground-based telescopes contributing to the COSMOS survey. 2) We discard candidate matches with a difference in brightness of more than 1.0 magnitude. 3) We finally select the matches as those with the smallest difference in angular positions. The COSMOS2015 magnitudes used in step 2) are measured in the Subaru *i*+ band within a fixed 3″ aperture (referred to as `ip_mag_aper3` in the catalogue). They are compared to the `SExtractor` magnitudes `MAG_BEST_HI` from ACS-GC which are defined as magnitudes measured within a flexible elliptical aperture (referred to as `MAG_AUTO`) or corrected isophotal magnitudes if contaminating sources are located in the vicinity. The median wavelengths weighted by transmission in the Subaru *i*+ and ACS F814W filters are 7683.88 Å and 8073.43 Å respectively, while the width and shape of their transmission curves differ significantly. These differences are accounted for by the relatively large tolerance in magnitude. We identify 98, 604 objects in the matched COSMOS2015 and ACS-GC catalog. From these matched objects 50 (95)% have less than 0.07 (0.22)″ and 0.12 (0.42) magnitude differences in their matched angular positions and luminosities respectively, which is well below the chosen tolerances described above and indicates that the match is robust. Subsequently we matched the joint COSMOS2015 and ACS-GC catalogue with the ZEST catalog using the same three-step method with the same tolerances for magnitudes and angular positions. The ACS-GC `MAG_BEST_HI` are now compared to the `SExtractor ACS_MAG_AUTO` provided in ZEST.

The final matched catalogue contains 70, 708 objects from which 50 (95)% have less than 0.03 (0.2)″ and 0.03 (0.16) magnitudes differences in their matched angular positions and luminosities respectively. These smaller differences compared to the first matching between COSMOS2015 and ACS-GC can be attributed to the fact that the positions and magnitudes used for the second matching are all derived with `SExtractor` from the same *HST* ACS imaging data. A second reason is the cut at $I_{AB} = 24$ in ZEST, which excludes the dimmest objects with highest uncertainties on position and luminosity estimates. This cut also explains the strong drop in the number of objects in the final catalogue.

2.1.5 *Volume limited main sample*

Our study is focused on disk-dominated late type galaxies in the matched catalogue, which we identify as those with ZEST parameters `type=2` and `bulg = 2 or 3`. Among them, we select a volume limited main sample adopting cuts in photometric redshift, absolute Subaru *i*+ magnitude and comoving effective radius. The selection is displayed in Fig. 2 and described in detail below. Examples of the galaxies in our main sample are shown in Fig. 1.

2.1.5.1 Redshift cuts. The redshift range of our main sample is set to $0.2 < z < 1.0$ (marked by vertical red dashed lines in Fig. 2). The upper limit is a compromise between a deep selection in redshift and a sufficiently high number of galaxies in the volume limited sample. The lower limit is defined by the end of the distribution, below which very few objects are found due to the small volume of the light cone. The redshifts on which the cuts are applied are the median of the likelihood distribution from the SED template fits, which are referred to as `photoz` in the COSMOS2015 catalogue.

2.1.5.2 Magnitude cuts. Galaxies are further selected to have apparent isophotal *AB* magnitudes in the Subaru *i*+ band (referred to as `ip_MAG_ISO` in the COSMOS2015 catalog and hereafter as m_i) brighter than $m_i^{\rm max} = 24$ above which the ZEST morphological classification becomes unreliable (Scarlata et al. 2007). The

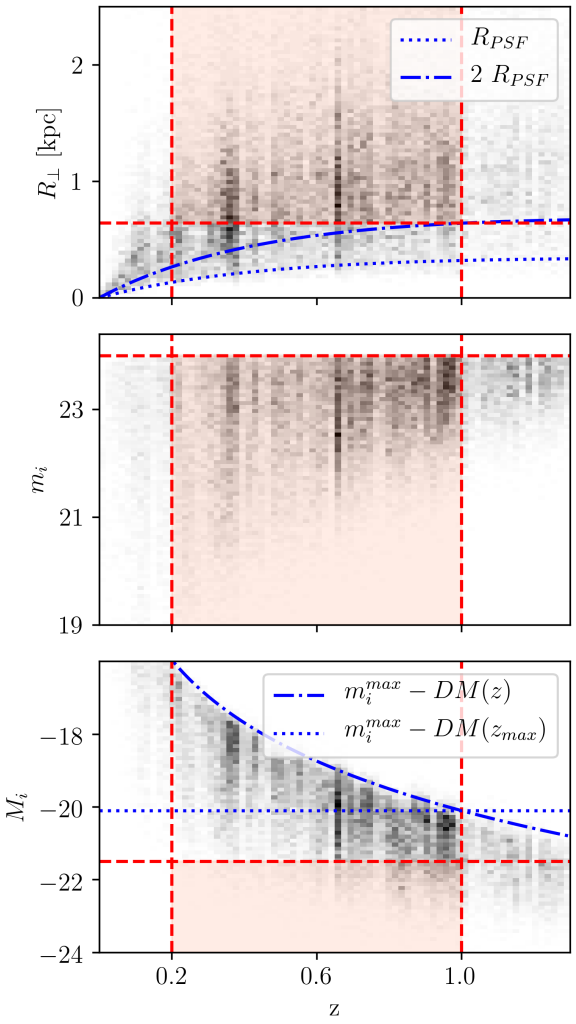

Figure 2. Selection of the volume limited main sample from disk dominated galaxies in the matched COSMOS catalogue by photometric redshift z, transverse comoving radii $R_\perp$ and apparent and absolute i band magnitudes m_i and M_i respectively. The cuts on each variable are marked by red dashed lines, enclosing the selected sample in the red area. The blue dotted and dashed-dotted lines in the top panel show the comoving radii which correspond to one and two times the angular size of the HST PSF respectively. The blue dashed-dotted line in the bottom panel shows the limit on M_i, given by the apparent magnitude cut m_i^{max} and the distance modulus DM. The horizontal blue dotted line in the same panel shows a naive cut on M_i (see text for details).

apparent magnitude cut introduces a redshift dependent selection by the absolute magnitude which hampers the comparison of galaxy populations at different redshifts (see bottom panel of Fig. 2). We therefore require the absolute restframe Subaru $i+$ magnitudes (hereafter referred to as M_i) to be brighter than $M_i^{\rm max} = -21.5$, ensuring that all objects in our redshift range are sufficiently bright to be unaffected by the apparent magnitude cut (Fig. 2). The choice of $M_i^{\rm max}$ is not straightforward due to uncertainties on the absolute magnitude estimate induced by dust extinction in the source galaxy, as illustrated in Fig. B1. In this figure we show the distribution of the $i - j$ rest frame color index as well as apparent i-band magnitudes versus the apparent two-dimensional axes ratios $q_{2D} \equiv B_{2D}/A_{2D}$ (provided as `BA_GALFIT_HI` in the ACS-GC) for the disk galaxies of our matched catalogue with $M_i < -21.5$ in three redshift bins. We see at all redshifts that galaxies with small apparent axes ratios are significantly redder (i.e. higher color index) and dimmer than those with apparent axes ratios close to unity. These effects can be expected from the extinction by dust in the interstellar medium of the source galaxy, as the pathway of light through the dust of the source towards the observer is longer for disks which are seen edge-on than for face-on objects (i.e. $q_{2D} << 1$ and $q_{2D} \simeq 1$ respectively). Dust extinction can hence shift disks with inclined orientations below the apparent magnitude limit, in particular at high redshifts, which was already pointed out in literature (e.g. Binney & de Vaucouleurs 1981; Huizinga & van Albada 1992). This can introduce a redshift-dependent bias in the observed distribution of axes ratios towards apparently round (face-on) disks, which could be mistaken for an evolution in the intrinsic shape distribution, if not taken properly into account. We demonstrate this effect in Fig. B1 by applying a cut at $m_i = 23$, as shown in the central panels. The apparent evolution of the axes ratio distribution introduced by this cut can be seen in the bottom panels of Fig. B1. An additional problem caused by this selection effect is that orientations of galaxies in samples affected by the apparent magnitude cut cannot be expected to be randomly distributed with respect to the observer, which violates a basic requirement for the 3D shape reconstruction method employed in this work.

In order to mitigate these dust extinction effects we select galaxies with absolute magnitudes which are sufficiently bright, such that their apparent magnitude is brighter than the selection cut, even if they are seen edge-on at the highest redshifts considered in this work. We find empirically, that this seems to be the case when selecting objects with absolute magnitudes of $M_i < -21.5$, as shown in the bottom panel of Fig. 3. The top panel of the same figure shows that a sample selected by a naive cut at $M_i^{\rm max} = m_i^{\rm max} - DM(z_{\rm max} = 1.0) = 20.1$ (indicated as blue dotted line in the bottom panel of Fig. 2) would lead to a biased axes ratio distribution since the m_i distribution is cut off at the apparent magnitude limit for $q_{2D} \lesssim 0.5$.

2.1.5.3 Size cuts. Our final selection addresses the sizes of galaxies. We require objects in our sample to have angular radii R_θ which are at least twice as large as the width of the PSF in the HST F814W imaging (i.e. $R_\theta^{\rm min} = 0.17''$) to minimize the effect of inaccuracies in the PSF correction on shape measurements as well as PSF effects on the morphological classifications (Scarlata et al. 2007; Griffith et al. 2012). Simply applying a cut on R_θ would lead to objects with smaller physical sizes entering the main sample at lower redshifts. This effect could introduce an apparent evolution of the galaxy shapes with redshift since the apparent physical sizes and shapes are correlated (see top panels of Fig. 4 and discussion below). We therefore apply a cut on the transverse comoving radii $R_\perp(z) = R_\theta D_A(z)$, which ensures that the observed angular radii of the galaxies in our sample are always larger than $R_\theta^{\rm min}$, even for the most distant objects at $z_{\rm max} = 1.0$. Here $D_A(z)$ is the angular diameter distance at the source redshift z. Assuming a flat ΛCDM universe we obtain the condition $R_\perp > R_\theta^{\rm min} D_A(z_{\rm max}) = 0.64$ kpc. The angular diameter distance D_A as well as the distance modulus DM are computed using cosmological parameters from the Planck Collaboration et al. (2018), i.e. $(\Omega_M, \Omega_b, H_0, \sigma_8, n_s) = (0.31, 0.049, 67.66, 0.81, 0.9665)$.

We show $R_\perp$ corresponding to one and two times the angular width of the HST PSF ($0.085''$) at a given redshift as dotted and dashed-dotted blue lines respectively in the top left panel of Fig. 2 together with the cut on $R_\perp$ which defines the main sample (red

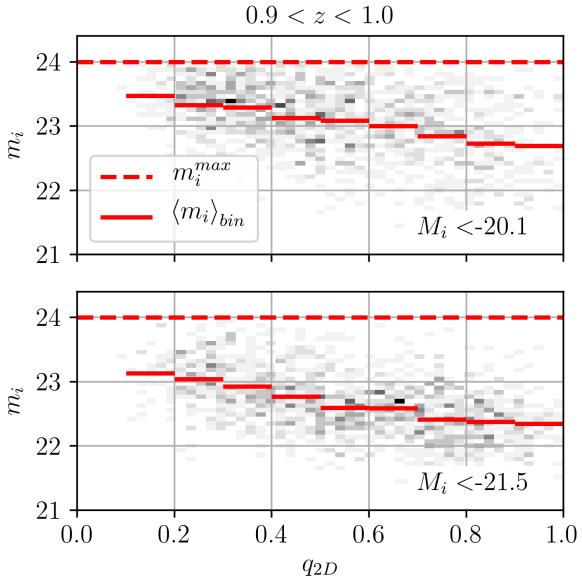

Figure 3. Apparent 2D axes ratios q_{2D} of disk dominated galaxies in COSMOS versus their apparent i-band magnitude m_i at the highest redshifts considered in this work. Horizontal bars show the average m_i in 10 q_{2D} bins to elucidate the correlation between both observables. Face-on disks with $q_{2D} \simeq 1$ appear brighter than edge-on disks, which indicates a dependence of dust extinction on the disk inclination relative to the observer. Top panel shows the volume limited sample selected as shown in Fig. 2, but with a more conventional cut on the absolute i band magnitude of $M_i < -20.1$. The m_i distribution of this sample is cut off at the apparent magnitude limit at $m_i = 24$, which biases the q_{2D} distribution, as illustrated in Fig. B1. We mitigated this bias with a more conservative cut of $M_i < -21.5$. The resulting sample, shown in the bottom panel, is only weakly affected by the cut on m_i.

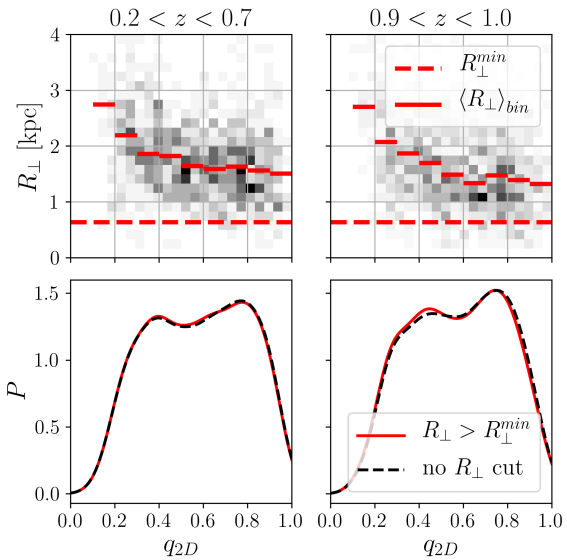

Figure 4. *Top*: Comoving transverse effective radii $R_\perp$ of disk dominated galaxies in our volume limited COSMOS sample verses the apparent 2D axes ratio q_{2D}. Red bars mark the average $R_\perp$ in bins of q_{2D} and show that the apparent size depends on the apparent axes ratio, presumably as an effect of the disk inclination. The horizontal dashed lines show minimum value for $R_\perp$ used as cut in our sample selection. *Bottom*: Distribution of q_{2D} for disk galaxies before and after the size cut (black dashed and red solid lines respectively). This figure demonstrates that our size cut does not bias the q_{2D} distribution of our sample.

dashed horizontal line). The angular radii R_θ are the PSF corrected effective radii from the `GALFIT` single Sèrsic model fits, which quantify the galaxy size along the projected major axes (referred to as `RE_GALFIT_HI` in the ACS-GC). For opaque disks with zero thickness the size of the projected major axes would be equal to the three-dimensional major axes, independent of its inclination with respect to the plane of projection. In that case a cut by projected size would not introduce a cut by shape or inclination with respect to the observer. However, real disk galaxies are not opaque but to a certain degree transparent. Their observed surface brightness profile is hence affected by projection effects, which depend on the inclination angle with respect to the observer. As a consequence the diameter of the observed 2D isophotes is larger for edge-on than for face on disks (e.g. Holmberg 1946; de Vaucouleurs 1959; Heidmann et al. 1972). In the top panels of Fig. 4 we show for galaxies brighter than our absolute magnitude cut that $R_\perp$ increases significantly with decreasing apparent axes ratios, indicating the expected dependence of $R_\perp$ on the disk inclination. However, for our bright sample and within the redshift range we consider, the lower limit on $R_\perp$ is sufficiently small to have only a negligible impact on the observed distribution of axes ratios as shown in the bottom panels of Fig. 4. We therefore do not expect a relevant impact of the size cut on the disk inclinations of our sample, which could otherwise bias the axes ratio distribution towards edge-on objects (e.g. Huizinga & van Albada 1992). All cuts defining the volume limited sample are summarized in Table 1. After applying these cuts the final volume limited main sample contains 3,739 disk dominated galaxies in total.

2.1.5.4 Type and color distributions. In Fig. 5 we compare the relative abundance of these disk galaxies with respect to the total population in three redshift bins of our volume limited sample. These abundances are compared to those of galaxies classified as disks with large bulges (ZEST parameter `type=2` and `bulg=0 or 1`), as elliptical (`type=1`) and irregular (`type=3`). The figure confirms reports from the literature that a large fraction of disks galaxies has no significant bulge. The fraction of disks remains roughly constant $\lesssim 80\%$, with a slight increase with redshift. It is further interesting to note, that at $z \simeq 1.0$ the majority of disks has no large bulge, while the opposite is the case at $z \simeq 0.4$. The declining fraction of bulgeless disks lines up with the findings from Sachdeva (2013) based on Chandra Deep Field observations and supports the scenario in which bulges form during mergers at lower redshifts. However, the absolute values of the different fractions may be specific to our sample selection. In particular the lower limit on the size separates out many elliptical galaxies, which tend to be more compact than disks.

For further validation of our data set we compare the color-color diagrams of the disk dominated and elliptical galaxies in our volume limited main sample in Fig. 6. We find that the disks and the ellipticals reside preferentially in the blue star forming and red quenched sequence respectively, which are well separated by the color-color cuts from Laigle et al. (2016). This result can be expected in general from the well known correlation between galaxy morphology and color (e.g. Larson et al. 1980; Strateva et al. 2001; Baldry et al. 2004; Martig et al. 2009). We find that the bulge dom-

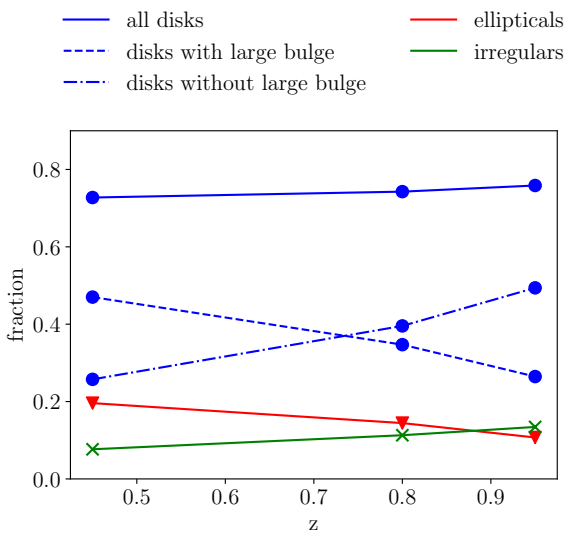

Figure 5. Fractions of galaxy types in our volume limited COSMOS sample in the three redshifts bins shown in Fig. 7. Blue circles, red triangles and green crosses show results for galaxies classified as disks, ellipticals and irregulars respectively. Results for disks with and without a large bulge are connected by dashed-dotted and dashed lines respectively.

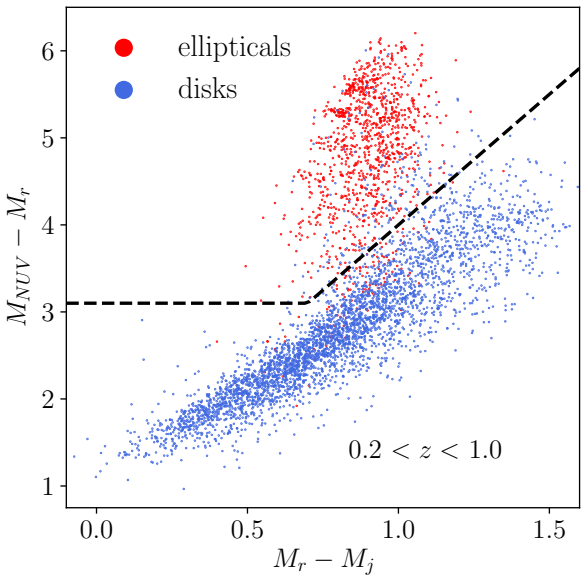

Figure 6. Color-color diagram, based on estimates of the absolute restframe magnitudes in the r, j and NUV filters from the COSMOS2015 catalogue for galaxies which pass our main sample selection on size, magnitude and redshift. Red and blue dots show objects which are classified in the ZEST catalogue as early type and disk dominated late-type respectively. The black dashed line is taken from Laigle et al. (2016) and separates the quenched and the star forming populations.

galaxy property	constraint
photometric redshift	$0.2 < z < 1.0$
apparent 3″ aperture AB Subaru i+ magnitude	$m_i < 24$
absolute rest-frame Subaru i+ magnitude	$M_i < -21.5$
transverse comoving effective radius	$R_\perp > 0.64$ kpc

Table 1. Selection cuts for the volume limited COSMOS main sample, shown in Fig. 2

inated disks in our sample populate both, the quenched as well as the star forming sequences (not shown in the figure for clarity). This result lines up with the large bulges found in disks on the red quenched sequence, for instance in data from COSMOS and the Sloan Digital Sky Survey (see Bundy et al. 2010; Guo et al. 2020). Overall, the expected correlation between color an morphology shown in Fig. 6 confirms a posteriori that the morphological classification from ZEST and the photometric properties from the COSMOS2015 are consistent with each other. This test shows that the matching between both catalogs is sufficiently reliable for deriving physical interpretations from their combined morphological and photometric information.

2.1.6 *Stellar mass - redshift samples*

In order to investigate the mass dependence of the intrinsic galaxy shapes we split the volume limited main sample into a low and and a high stellar mass sample at $M_\star^{\rm cut} = 10^{10.35} {\rm M}_\odot$, which is close to the main samples median stellar mass. Each mass sample is further split into three redshift sub-samples to study the evolution of the shapes. The width of the redshift bins are chosen such that each sample contains a sufficiently large number of objects required for our statistical analysis. The redshift and stellar mass distributions are shown with the corresponding cuts in Fig. 7 and 8 respectively.

The cuts in mass and redshift are summarized in Table 4 together with the number of galaxies in each sub-sample.

We show in the left column of Fig. 9 the distribution of the observed shapes from the ACS-GC catalog, quantified by the axes ratio q_{2D}, in the three redshift bins. We find that at all redshifts the distributions of the low and high mass samples are skewed towards high and low 2D axes ratios respectively. The difference between the mass samples increases with decreasing redshifts, which is mainly driven by an increasing fraction of high mass galaxies with low 2D axes ratios ($q_{2D} \simeq 0.3$). The axes ratio distribution of low mass galaxies on the other hand shows no strong change with redshift. In fact, we argue in Section 4 that the redshift dependence of both samples is not significant when considering shot-noise errors on the measurements. Nevertheless, a weak trend in redshift can also be seen in the transverse comoving radii $R_\perp$ in the central column of Fig. 9. These radii are shown for disks inclined towards a face-on orientation with apparent axes ratios $q_{2D} > 0.5$ to reduce the impact of inclination on the observed size (see Fig. 4). As for the axis ratios we find that at high redshift, the size distribution for low and high mass samples is similar. At lower redshift, the deviation between both distributions is slightly larger, mainly due to an increase of the sizes in the high mass disk sample. This trend can be seen in the average radii, displayed as dotted and dash-dotted vertical lines for the high and low mass sample, respectively.

A non-geometric galaxy property which follows the same behaviour is the specific star formation rate ($sSFR$) from the COSMOS2015 catalogue, whose distribution is displayed in the right column of Fig. 9. The selection here is again restricted to galaxies with $q_{2D} > 0.5$ to mitigate a potential bias in the $sSFR$ estimates induced by inaccuracies of dust attenuation model employed in the SED fitting, as reported by Laigle et al. (2019). We see that the $sSFR$ distribution is similar for the low and high mass samples at high red-

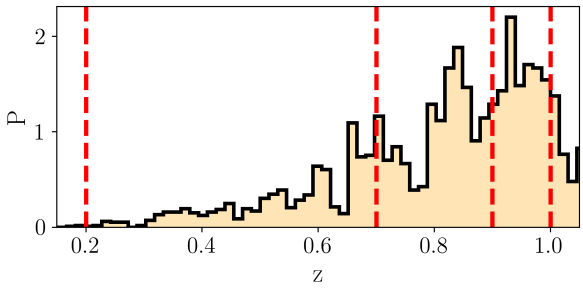

Figure 7. Selection of redshift sub-samples in COSMOS. The photometric redshift distribution of disk dominated galaxies in the volume limited main sample is split into three redshift bins, which are enclosed by vertical red dashed lines at $z = 0.2, 0.7, 0.9$ and 1.0.

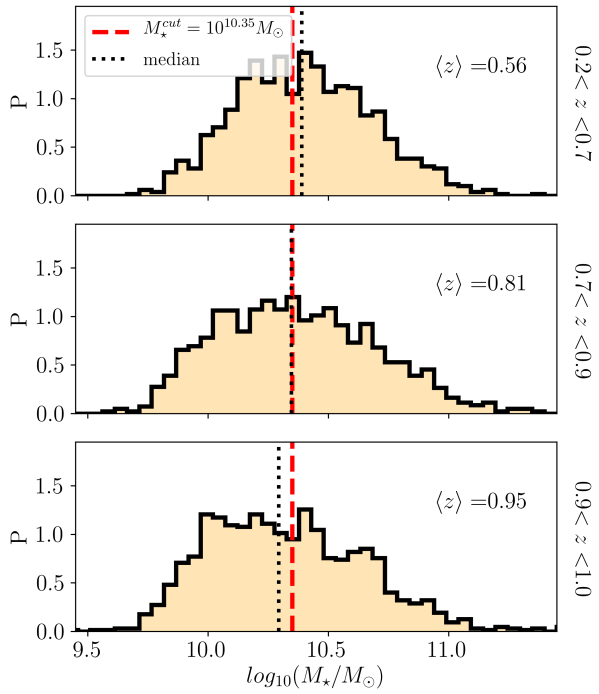

Figure 8. Selection of stellar mass sub-samples in COSMOS. The stellar mass distributions of the three redshift samples from Fig. 7 are split into a high and low mass sample at the redshift independent cut marked by the red dashed lines. This cut lies close to the median stellar masses of the different redshift samples, which are marked as black dotted lines.

shift. At low redshift, both distributions differ significantly, which is mainly driven by a strong decrease of the $sSFR$ for high mass disks. This result lines up with those of Grossi et al. (2018), who find that the $sSFR$ of disk dominated galaxies in COSMOS field decreases with increasing stellar mass and decreasing with redshift. Overall, these findings indicate a correlation of the galaxy shapes, sizes and specific star formation rates with the stellar masses, which appear to increase as galaxy formation proceeds. We will discuss this finding in more detail together with the reconstructed 3D axes ratio distribution in Section 5.

2.2 Disk galaxies in hydro-dynamic simulations

We use the state-of-the-art hydrodynamic simulations of galaxy formation Horizon-AGN[5] and Illustris TNG100[6] (hereafter referred to as HAGN and TNG100, respectively) to test the methods and assumptions on which our analysis of the COSMOS data is based on. These tests are performed at redshift $z = 1.0$, were the available snapshots of these simulations are closest to the maximum of the redshift distribution of our volume limited COSMOS sample. Both simulations assume a ΛCDM cosmology with recently constrained parameters, cover similar cosmological volumes and include the same mechanisms to model the formation of galaxies as detailed below. However, their simulation techniques differ significantly, which allows for testing the robustness of our conclusions. The main characteristics of these simulations are compared to each other in Table 2. Note that these simulations where run at relatively low resolutions in order to cover large volumes, which has a noticeable impact on the galaxy morphologies as discussed in Section 3.1.

2.2.1 *Horizon AGN*

The hydrodynamic simulation HAGN was produced with the grid-based adaptive-mesh-refinement code RAMSES (Teyssier 2002), using cosmological parameters compatible with the constraints from WMAP-7 (Komatsu et al. 2011). The simulation includes the key processes relevant for galaxy formation: cooling, heating and chemical enrichment of gas, the formation and evolution of stars and black holes as well as feedback from stellar winds, supernovae and Active Galactic Nuclei (AGNs) (Dubois et al. 2014). Galaxies were identified in the distribution of stellar particles as groups with more than 50 members using the AdaptaHOP finder (Aubert et al. 2004). A reasonable agreement with observed luminosity functions and color distributions has been shown by Kaviraj et al. (2017), Dubois et al. (2016) report realistic galaxy morphologies, while moderate deviations from observed angular clustering have been found by Hatfield et al. (2019).

For our analysis we select disk galaxies, which we define via the ratio $r_v = V_{rot}/\sigma_v$ between the stellar rotation V_{rot}, defined as the mean tangential velocity of star particles with respect the galaxies spin axis and the velocity dispersion σ_v (see Chisari et al. (2015) for details). High values of r_v indicate relatively high rotational velocities compared to those radial or parallel to the spin axes. For our analysis we select the 20% of galaxies with the highest values of r_v, which corresponds to a cut at $r_v > 1.06$ at redshift $z = 1.0$ (Fig. 10). We attribute this low value of r_v to the relatively low resolution of the simulation and demonstrate in Section 3.1 that the selected galaxies are indeed disky, although with "puffed-up" shapes, characterized by relatively high C_{3D}/A_{3D} axes ratios. We further limit the selection to galaxies with more than 500 particles, which corresponds to a stellar mass cut at $M_\star > 10^9 M_\odot$, to ensure reliable measurements of the morphological properties (see also Section 2.2.3). The final sample contains 14198 disk galaxies.

2.2.2 *Illustris TNG100*

The TNG100 (Springel et al. 2018; Naiman et al. 2018; Nelson et al. 2018; Marinacci et al. 2018; Pillepich et al. 2018b) is a magneto-hydrodynamic simulation, produced with the moving-mesh code

[5] www.horizon-simulation.org
[6] www.tng-project.org

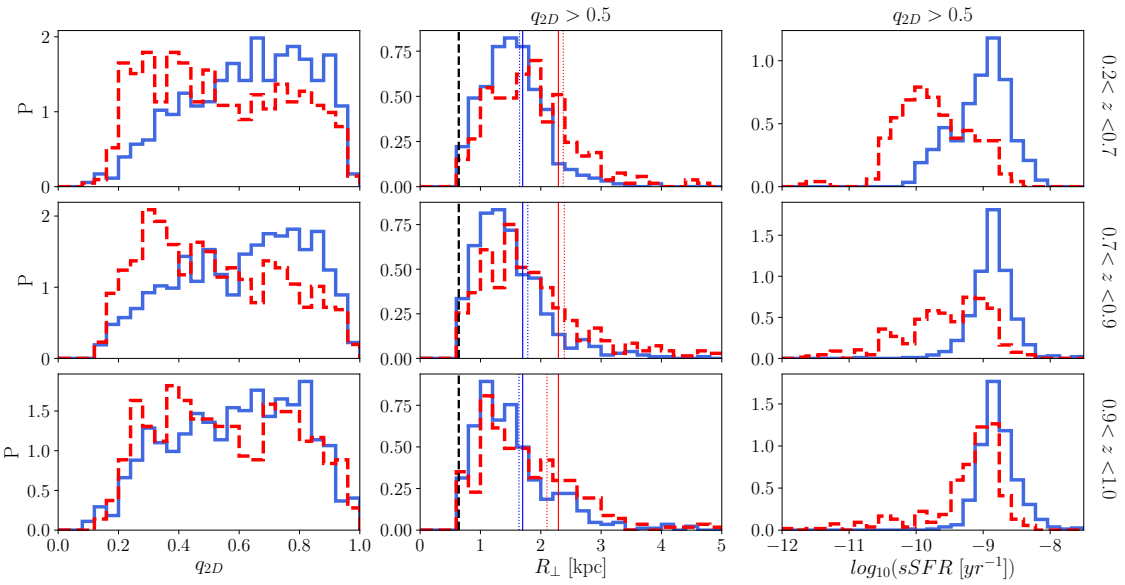

Figure 9. Probability distributions of apparent 2D axes ratios, transverse comoving radii and specific star formation rates (left, central and right panels respectively) for disk dominated galaxies in our volume limited COSMOS main sample with stellar masses below and above $10^{10.35}$M$_\odot$ (blue and red histograms respectively). Vertical panels show results in three redshift bins with limits indicated on the right. The comoving radii and specific star formation rates are shown for disks with apparent axes ratios above $q_{2D} > 0.5$, to minimize bias induced by projection and dust extinction (see Fig. 4 and B1). Vertical black dashed lines mark the minimum radius of the volume limited sample. Vertical solid and dotted lines indicate the mean radii for each mass sample over the full redshift range and in each redshift bin respectively.

AREPO (Springel 2010), which was run with cosmological parameters from the Planck Collaboration et al. (2016). It includes the same key processes for modeling galaxy formation as HAGN, although with significantly different implementations which are described in Pillepich et al. (2018a). Galaxies are identified in dark matter subhaloes with non-zero stellar components. These subhaloes are detected in friends-of-friends groups by the SUBFIND algorithm (Davis et al. 1985; Springel et al. 2001; Dolag et al. 2009). The simulation has been shown to reproduce main characteristics of observed galaxy populations reasonably well, such as morphologies (Rodriguez-Gomez et al. 2019), stellar mass functions (Pillepich et al. 2018b), the color bimodality (Nelson et al. 2018) as well as color-dependent two-point clustering statistics (Springel et al. 2018). The basic properties of the simulation are compared to those of the HAGN simulation in Table 2.

To identify disks in the TNG100 simulation we use each galaxy's fraction of stellar mass in the disk component with respect to the total stellar mass. For this purpose stellar disk particles have been defined via their circularity parameter $\epsilon \equiv J_z/J(E)$, where J_z is the specific angular momentum around a selected z-axis and $J(E)$ is the maximum specific angular momentum possible at the specific binding energy E of the star. The z-axis is selected with respect to the star forming gas, or the stars, if there is no star forming gas in the system (Vogelsberger et al. 2014; Genel et al. 2015). Particles with $\epsilon > 0.7$ are considered to belong to the disk component (Abadi et al. 2003). The circularity parameter is provided on the Illustris database for all subhalos with $M_\star > 3.4 \times 10^8M_\odot$ within the half mass diameter 2 $R_{1/2,\star}$ and at least 100 stars. We classify TNG100 galaxies as disks if their fraction of disk particles is above 0.35, which corresponds to the upper 20% of the distribution at $z = 1.0$, as shown in Fig. 10. As for HAGN, we attribute this low fraction of disk particles used for the cut to the limited resolution of the simulation and demonstrate in Section 3.1 that it is a reasonable choice for selecting disky objects. Note that we choose the disk particle fraction for the morphological classification in TNG100 since this quantity is provided for the $z = 1.0$ snapshot on the public TNG database in contrast to r_v. Besides this practical motivation, using two different morphological classification schemes in both simulations allows for drawing more robust conclusions regarding the validation of our analysis methods. The final sample contains 5674 disk galaxies.

		TNG100	HAGN
Ω_Λ	-	0.6911	0.728
Ω_m	-	0.3089	0.272
Ω_b	-	0.0486	0.045
H_0	[s^{-1}km]	67.74	70.4
σ_8	-	0.8159	0.81
n_s	-	0.9667	0.967
$L_{\rm box}$	[h^{-1}Mpc]	75	100
$m_\star$	[M$_\odot$]	-	2×10^6
$m_{\rm baryon}$	[M$_\odot$]	1.4×10^6	-
$m_{\rm dm}$	[M$_\odot$]	7.5×10^6	8×10^7

Table 2. Main properties of the hydro-dynamic simulations Illustris TNG 100 and Horizon AGN.

2.2.3 *Axes ratio measurements*

The galaxies axes ratios provided for the HAGN and TNG100 simulations are computed from the moment of inertia of their stellar

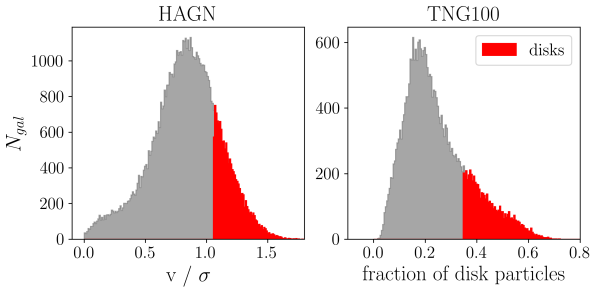

Figure 10. *Left*: Distribution of the ratio between stellar rotation $V_{\rm rot}$ and the velocity dispersion σ_v for galaxies in the HAGN simulation. *Right*: Distribution of the fraction of disk particles in each galaxy of the TNG100 simulations. The populations of galaxies which we classify as disks are marked in red at the tails of the distributions, and make up 20 % of the entire sample. Results are shown for $z = 1.0$.

mass distributions

$$I_{i,j} \equiv \frac{1}{M_\star} \sum_n^{N_\star} m_\star^n r_i^n r_j^n, \tag{4}$$

where $N_\star$ is the number of stellar particles in the galaxy, $m_\star^n$ is the stellar mass of the $n^{\rm th}$ particle, $M_\star = \sum_n^{N_\star} m_\star^n$, and r_i^n are the components of the particle position vectors, defined with respect to the center of mass and (Chisari et al. 2015; Genel et al. 2015).

The moment of inertia can be defined via the particle positions in 3D as well as in 2D. In the latter case the positions are projected along one coordinate axis of the simulation, assuming an observer at infinity. In the 3D case the square roots of the three absolute eigenvalues $\lambda_1 \geq \lambda_2 \geq \lambda_3$ provide a measure of the 3D major, intermediate and minor axes lengths, respectively, i.e. $(A_{3D}, B_{3D}, C_{3D}) = \sqrt{(\lambda_1, \lambda_2, \lambda_3)}$. Accordingly, the 2D major and minor axes lengths are given by $(A_{2D}, B_{2D}) = \sqrt{(\lambda_1, \lambda_2)}$ respectively. The axes ratios are defined according to equation (1) and (2). We expect that the bias on such axes ratio measurements, which results from the discreteness of the particle distributions (e.g. Joachimi et al. 2013; Hoffmann et al. 2014; Chisari et al. 2015), is negligible, due to the lower mass limits imposed on our sample (see Section 2.2.1 and 2.2.2). The 2D axes ratios of the projected stellar mass distributions in HAGN are used to test our method for reconstructing the 3D axes ratio distribution. For the TNG100 such measurements are currently not publicly available. However, we use 2D axes ratios measured in synthetic images from TNG100 galaxies from Rodriguez-Gomez et al. (2019). These images have been produced using the SKIRT radiative transfer code and take into account the effects of dust attenuation and scattering, mimicking PSF-convolved observations by the Sloan Digital Sky survey in the g and i broad band filters. The axes ratios are obtained from the second order moments of these images. Since these measurements are not PSF-corrected, we do not use them for testing the shape reconstruction method. Instead, we use them to obtain a rough estimation of how strongly the observed galaxy shapes depend on the wavelength range in which they are measured in order to interpret the COSMOS observations.

3 RECONSTRUCTING 3D GALAXY SHAPE DISTRIBUTIONS FROM 2D OBSERVATIONS

We infer an estimate of the 3D axes ratio distribution of a given galaxy sample from the distribution of the observed 2D axes ratios, using a variation of a method which has been widely used in the literature (see references below). We assume that each galaxy in the sample can be represented by an absorption-free, self-similar, coaxial ellipsoidal stellar system, to which we refer to as 3D ellipsoid in the following. The shape of its 3D luminosity density is fully described by the two axes ratios q_{3D} and r_{3D}, given by equation (1). We expect such a one-component model to be a simplistic, but useful description for the objects in our observed sample: disk-dominated galaxies, discarding bulge-dominated and irregular objects (see Section 2.1.3). However, substructures such as spiral arms could bias our results (see Fig. 1). The isodensity contours of the projected luminosity density (i.e. the isophotes) of such model galaxies are self-similar, coaxial ellipses (Stark 1977), whose 2D axis ratios can be obtained from the 3D axes ratios analytically, as detailed in Appendix A. This allows for an efficient prediction of the 2D axes ratio distribution, $P(q_{2D})$, for an ensemble of randomly oriented model galaxies with a given distribution of 3D axes ratios, $P(q_{3D}, r_{3D})$. The latter can hence be constrained by comparing the $P(q_{2D})$ prediction to observations. This approach relies on a physically meaningful model for $P(q_{3D}, r_{3D})$, which we motivate in Section 3.1. The free model parameters are obtained from the COSMOS data using Bayesian interference as detailed in Section 3.2 and 3.3. In the latter section we also study the impact of inaccuracies of the employed $P(q_{3D}, r_{3D})$ model on the inferred 3D axis ratio distribution.

3.1 Model for the 3D axes ratio distribution

The reconstruction of 3D axes ratio distributions relies on a physically meaningful model for those distributions. Several of such models have been proposed in the literature. Sandage et al. (1970) found that the q_{2D} distribution of spiral galaxies can be fitted reasonably well with a simple oblate disk model according to which $q_{3D} = 1$ for all objects while s_{3D} is normal distributed around $\langle s_{3D} \rangle \simeq 0.25$. Later studies based on larger samples found that the q_{2D} distribution of spirals is better fitted using slightly triaxial disk models which describe the absence of perfectly circular face-on spirals in observations (e.g. Binney & de Vaucouleurs 1981; Fasano et al. 1993). Using normal distributions for q_{3D} and s_{3D} Lambas et al. (1992) obtained good fits to the observations from the APM Bright Galaxy Survey. The good performance of this model has been confirmed by recent results from Satoh et al. (2019) based on COSMOS data. Ryden (2004) found that a normal distribution for s_{3D} and a log-normal distribution for the ellipticity $\epsilon_{q_{3D}} \equiv 1 - q_{3D}$ delivers good fits to the the q_{2D} distribution of spirals in SDSS observations, which was confirmed by later studies (e.g. Padilla & Strauss 2008; Rodríguez & Padilla 2013). An alternative model based on normal distributions of the ellipticity $\epsilon_{s_{3D}} \equiv 1 - s_{3D}$ and the triaxiality $T \equiv (1 - q_{3D}^2)/(1 - s_{3D}^2)$ proved to match the q_{2D} distribution from SDSS, 3D-HST, COSMOS and CANDELS observations (Chang et al. 2013; van der Wel et al. 2014).

These different models were motivated mainly by the fact that their prediction for the 2D axes ratios (or ellipticities) fit observations reasonably well, which indicates that observations do not provide a strong constrain on the functional form of the 3D axes ratio distribution. This limitation can be overcome with a direct validation of the model using axes ratio distributions of galaxies from hydrodynamic simulations in cosmological volumes. To our knowledge such a validation has not been presented in the literature so far and is therefore subject of this work. For this purpose we use the HAGN and TNG100 simulations, described in Section 2.2. Since cosmological hydrodynamical simulations reproduce ob-

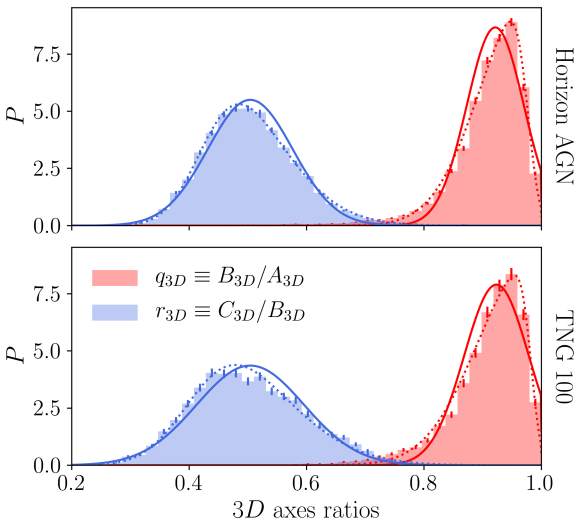

Figure 11. Distributions of 3D axes ratios for disk galaxies in hydrodynamic simulations at $z = 1.0$, obtained from the simple moment of inertia. Solid and dotted lines show fits to a normal and a skew normal distribution respectively.

served galaxy morphologies to varying degree of success and with a known dependence on simulation techniques, sub-grid models and resolution (Snyder et al. 2015; Dubois et al. 2016; Correa et al. 2017; Park et al. 2019; Rodriguez-Gomez et al. 2019; Tacchella et al. 2019), we only use them as a tool to validate our reconstruction method.

In Fig. 11 we show the marginalized probability distributions of q_{3D} and r_{3D} for galaxies classified as disks in the HAGN and TNG100 simulations (see Section 2.2 for details). We find that the disks tend to be oblate with $r_{3D} < q_{3D} \lesssim 1$ in both simulations, indicating that the morphological classification is reasonable. Note that the absence of thin disks with $r_{3D} << 1$ can be attributed to the relatively low resolution of these simulations, while they are present for instance in the TNG50 run (see Pillepich et al. 2019) or the New Horizon Simulation (Park et al. 2019), which are higher resolution versions of the runs analysed here.

We fit the probability distributions with normal and skew normal distributions, given by $G(x) \propto \exp\{-\delta_x^2\}$, and $G_s(x) = G(x)(1 + \mathrm{erf}\{\gamma\delta_x\})$ respectively, with $\delta_x \equiv (x - x_0)/(\sqrt{2}\sigma)$ [7]. Both functions are truncated outside of the interval $[0, 1]$ to ensure that $A_{3D} \geq B_{3D} \geq C_{3D}$. We show in Fig. 11 that the fit of the skew normal distribution matches the axes ratios slightly better than the normal distribution, in particular q_{3D}. However, we decide to neglect the skewness in our modeling, since the improvement in the 3D axes ratio fits is relatively small. In addition, we find that a skewness on q_{3D} has a very minor impact on the corresponding distribution of q_{2D} and could hence be constrained very poorly by observations (see Fig. A2). A model for the joint distribution of q_{3D} and r_{3D} would not only need to approximate the marginalized probability distributions of both axes ratios, but also of a potential correlation between them. We therefore inspect the joint distribution of q_{3D} and r_{3D} for such a correlation in Fig. A1 and find no evidence for a significant correlation between these two axes ratios in both simulations. Note that this is not necessarily the case for elliptical galaxies, and joint distribution of other parameters, commonly used in the literature to quantify galaxy shapes, as discussed previously. Based on these findings we approximate the joint 3D axes ratio distribution with the product $G(q_{3D})G(r_{3D})$, i.e.

$$\tilde{P}(q_{3D}, r_{3D}) = \exp\left\{-\frac{1}{2}\left[\left(\frac{q_{3D} - q_0}{\sigma_q}\right)^2 + \left(\frac{r_{3D} - r_0}{\sigma_r}\right)^2\right]\right\}, \quad (5)$$

where q_0, σ_q, r_0, σ_r are the free parameters of the model. The normalized truncated distribution is then given by

$$P = \begin{cases} \tilde{P}_{3D}/\mathcal{N} & \text{if } q_{3D}, r_{3D} \in (0, 1] \\ 0 & \text{else} \end{cases} \quad (6)$$

with $\mathcal{N} = \int_0^1 \int_0^1 \tilde{P}_{3D}(q_{3D}, r_{3D})\, dr_{3D}\, dq_{3D}$. A distribution of axes ratios drawn from this model with the parameters obtained from the fits shown in Fig. 11 is compared to the HAGN and TNG100 simulations in Fig. A1. The model matches the simulation results reasonably well for both types of galaxies, although we find a $\simeq 10\%$ offset in the maximum of the distributions, which could presumably be reduced by adding a skewness as an additional parameter as discussed above.

3.2 Error estimation and parameter inference

We obtain constraints on our model parameter vector $\boldsymbol{\theta} = (q_0, \sigma_q, r_0, \sigma_r)$ from the observed data using Bayesian inference. We assume a multivariate normal distribution of the likelihood for observing the data vector $\mathbf{d}$ given the parameters $\boldsymbol{\theta}$,

$$\ln \mathcal{L}(\mathbf{d}|\boldsymbol{\theta}) = -\frac{1}{2}\chi^2(\mathbf{d}|\boldsymbol{\theta}) + const. \quad (7)$$

with

$$\chi^2(\mathbf{d}|\boldsymbol{\theta}) = [\mathbf{d} - \mathbf{m}(\boldsymbol{\theta})]^\mathsf{T} C^{-1} [\mathbf{d} - \mathbf{m}(\boldsymbol{\theta})] \quad (8)$$

The data vector is the observed distribution $P(q_{2D})$, measured in 25 bins of equal width within the q_{2D} interval $[0, 1]$ and $m(\boldsymbol{\theta})$ is the corresponding prediction from our $P(q_{3D}, r_{3D})$ model for the parameters $\boldsymbol{\theta}$. The posterior distribution of the parameters $\boldsymbol{\theta}$ given the data $\mathbf{d}$ is given by Bayes' theorem as

$$P(\boldsymbol{\theta}|\mathbf{d}) \propto \mathcal{L}(\mathbf{d}|\boldsymbol{\theta})\Pi(\boldsymbol{\theta}), \quad (9)$$

where is $\Pi(\boldsymbol{\theta})$ is the prior, which we set to be flat in the intervals $[0, 1]$ and $[0.01, 1]$ for the parameters (q_0, r_0) and (σ_q, σ_r) respectively. The covariance matrix C between the different bins of the data vector is assumed to be diagonal, given by $C_{ij} = \delta_{ij}\, \sigma_i^2$, with Poisson shot noise variance $\sigma_i^2 \propto N_i$ where N_i are the counts of galaxies in a given bin i. The model prediction $m(\boldsymbol{\theta})$ is obtained by drawing a sample of 3D axes ratio pairs (q_{3D}, r_{3D}) from the $P(q_{3D}, r_{3D})$ distribution for a given set of parameters $\boldsymbol{\theta}$. The corresponding q_{2D} axes ratios are then computed for a random orientation, as detailed in Appendix A. The prediction for $P(q_{2D})$ is measured from the resulting q_{2D} sample in the same bins as the observed data. For generating the predictions we choose a sample size of 10^5, which is a compromise between a fast computation, needed for efficiently estimating the posterior, and having errors on the prediction which are negligible compared to those on the data vector. The latter condition is satisfied, as the number of galaxies in our six COSMOS sub-samples is more than two magnitudes smaller than the samples used for generating the predictions (see

[7] The fits are obtained by minimizing the χ^2 deviation between model and data, assuming shot noise errors on the latter.

Table 4). We estimate $P(\boldsymbol{\theta}|\mathbf{d})$ by sampling the parameter space with the Markov-Chain-Monte-Carlo (MCMC) method using the code `emcee`[8] (Foreman-Mackey et al. 2013). For each posterior we run 32 independent chains with at last 1000 steps each. The best fit parameters are obtained from the position of the maxima of the marginalized posterior distribution.

3.3 Testing the reconstruction method

The method for reconstructing the distribution of 3D axes ratios $P(q_{3D}, r_{3D})$ from the distribution of 2D axes ratios $P(q_{2D})$ is now tested using the HAGN simulation. We begin by validating two assumptions on which this method is based on. Those are a) that the galaxies 3D stellar mass isodensities are coaxial, self-similar 3D ellipsoids, whose 3D axes ratios can be related analytically to the 2D axes ratios of the projected stellar masses as described in Appendix A, assuming random orientations and b) that our Gaussian model for the 3D axes ratio distributions from equation (6) is sufficiently accurate to provide good predictions for the 2D axes ratio distribution. Subsequently, we test how well the distribution of 3D axes ratios in the simulation can be recovered from the corresponding distribution of 2D axes ratios.

To test assumption a) we compare in Fig. 12 the q_{2D} distribution in the HAGN simulation, measured directly from the projected distributions of each galaxies stellar particles as described in Section 2.2.3, to the distribution of 2D axes ratios, obtained analytically from each galaxies 3D axes ratios (top and central panel respectively). We find that both distributions differ significantly from each other, which indicates that the assumption of ellipsoidal stellar mass isodensities can only serve as a very rough approximation. This conclusion can already be expected from the images of face-on late-type galaxies in our COSMOS sample, shown in Fig. 1. However, certain characteristics are present in both distributions, such as the cut-offs at $q_{2D} \simeq 0.4$ and $q_{2D} \simeq 0.9$, as well as a skewness in the distributions towards lower axes ratios. To test assumption b) we show in the bottom panel of Fig. 12 the q_{2D} distribution predicted for an ensemble of 10^6 3D axes ratios, drawn from our $P(q_{3D}, r_{3D})$ model fit to the HAGN simulation (see Fig. 11 and A1). We find that this predicted distribution is in reasonable agreement with the results obtained from the analytical projection of 3D axis ratios, which indicates that our Gaussian model for $P(q_{3D}, r_{3D})$ from equation (6) might be an appropriate approximation for our analysis.

We study the performance of the reconstruction method, starting with a self consistency test in which we fit the $P(q_{3D}, r_{3D})$ model to match its own $P(q_{2D})$ prediction, using parameters from the HAGN fits shown in Fig. 12. We find that the fit, shown as green line in the bottom panel of Fig. 12, is in good agreement with the reference measurements. The MCMC estimate of the posterior distribution is displayed in Fig. 13 as light and dark green contours, indicating the 68% and 95% confidence intervals, respectively. We find that the parameter constraints are in good agreement with the input parameters of the $P(q_{3D}, r_{3D})$ model, shown as black dashed lines in the same figure. This result demonstrates that the 3D axes ratio distribution can be reconstructed from the corresponding distribution of 2D axes ratios for a sample of idealised disk galaxies, which satisfy the model assumptions outlined above. Note that this is not necessarily the case for elliptical galaxies, which are not subject of this work.

We perform the same test under more realistic conditions by fitting the q_{2D} distribution obtained by the projection of idealized 3D ellipsoids with axes ratios measured from HAGN galaxies. The fit, shown as red line in the central panel of Fig. 12, is in an good agreement with the corresponding measurements. We attribute the remaining deviations to inaccuracies of the $P(q_{3D}, r_{3D})$ model and not to the assumption of ellipsoidal stellar mass isodensities used for obtaining the 2D axes ratios, since this assumption is employed for generating both the prediction as well as the reference measurements. The parameter constraints, shown as red contours in Fig. 13, are significantly biased with respect to the reference parameters from the $P(q_{3D}, r_{3D})$ model fits to the 3D axes ratio distribution in HAGN. However, the relative deviations of the best fits (defined as maxima of the marginalized probabilities) are at the percent level for q_0, r_0 and σ_r (see Table 3). The σ_q parameter shows the strongest deviation from the reference values of more than 100%.

Our most realistic performance test of the reconstruction method consists in fitting the model to the distribution of 2D axes ratios measured from each galaxy's projected stellar mass distribu-

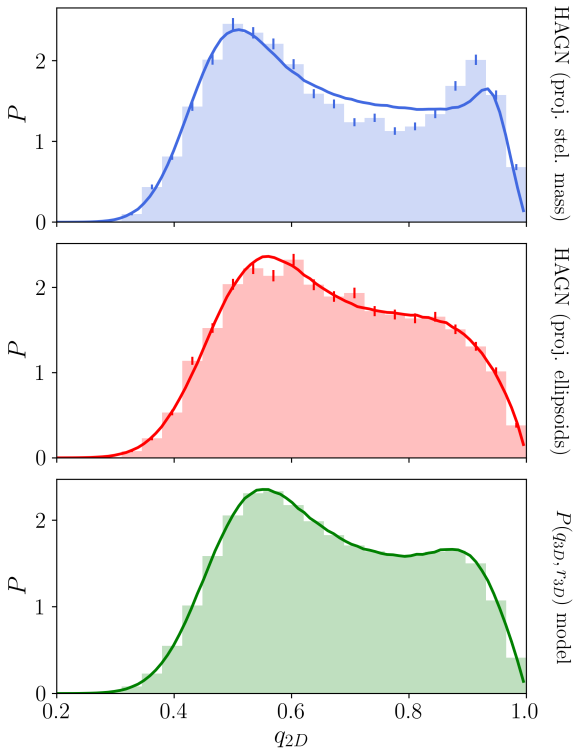

Figure 12. Probability distribution of 2D axes ratios. Top and bottom panels show results from the HAGN simulation, measured from the projected stellar mass distributions and analytic projections derived from 3D axes ratios, assuming coaxial, self-similar ellipsoidal stellar mass isodensities respectively. The bottom panel shows the 2D axes ratio distribution predicted by the Gaussian model for the 3D axes ratio distribution with parameters from the 3D fits, shown in Fig. 11. In each panel we show fits of the model prediction as solid lines. The corresponding parameter constraints and best fit values are compared in Fig. 13 and Table 3. Poisson shot-noise estimates of the standard deviation are shown as error bars on each bin and are smaller than the line width in the bottom panel.

[8] emcee.readthedocs.io

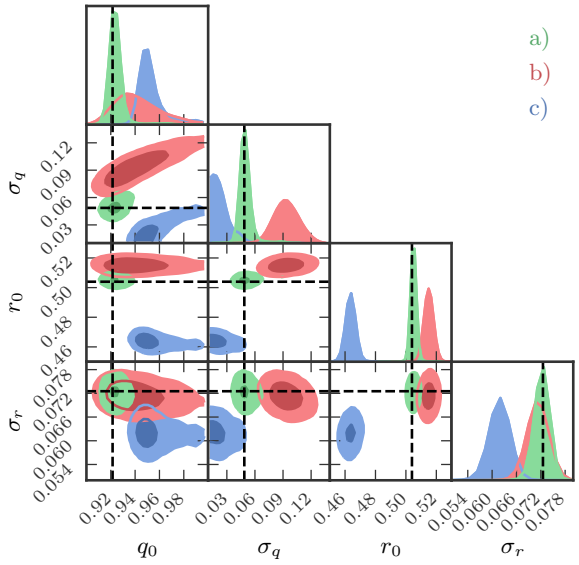

Figure 13. Parameter constraints derived from a) an ensemble of projected ellipsoids with 3D axes ratio distributions following the Gaussian model from equation (7) and (8), b) projected 3D ellipsoids with 3D axes ratio distributions of disk galaxies in the HAGN simulation c) projected stellar mass distributions of HAGN disks.

tion. We find that the fit, shown as blue line in the top panel of Fig. 12, strongly deviates from the corresponding measurements. This finding can be expected from the previously discussed deviation between the q_{2D} distribution from the 3D axes ratios and the projected stellar mass distributions as the 3D axes ratio projection is employed in the modeling of the q_{2D} distribution. However, some main characteristics, such as the cut-off of the distribution, the position of the local maxima, and the skewness towards low axes ratios, are captured by the fit. We find that the parameters constraints, shown as blue contours in Fig. 13 are biased more significantly with respect to the reference values from the direct $P(q_{3D}, r_{3D})$ model fits compared to the previous test case, except for σ_q. Also, the relative deviations of the absolute values tend to be higher than those from the q_{2D} distribution from the analytic projection assuming ellipsoidal stellar mass distributions (see Table 3). Based on these results we expect an accuracy on the reconstructed model parameters of less than 5%, 10%, 65% and 15% for q_0, r_0, σ_q and σ_r, respectively. It is worth noting that these results may be overly pessimistic since we used all disk galaxies in HAGN, including those with large bulges for which a one-component ellipsoidal model is presumably inaccurate.

The uncertainties on the reconstructed σ_q are too high for drawing meaningful conclusions when analysing observational data. This is illustrated in Fig. 14, where we compare the reconstructed distributions for q_{3D} and r_{3D} directly with the the HAGN measurements. The location of the maxima of the reconstructed distributions of q_{3D} and r_{3D}, given by the model parameters q_0 and r_0, are close to the positions of the maxima in the measurements. However, the width of the reconstructed distributions differs strongly from the measurements. The significance of these deviations is specific to the sample size, which determines our shot noise error estimate on q_{2D}. The bias on our observational constraints can be expected to be less significant with respect to the errors than in our test cases, as the sample sizes are roughly one order of magnitude smaller.

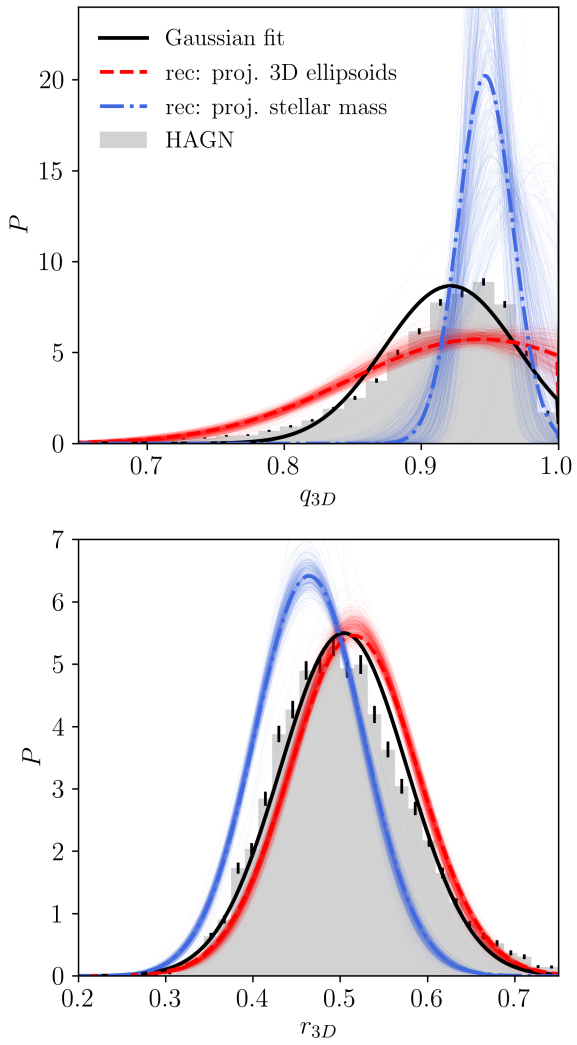

Figure 14. Reconstruction test of 3D galaxy axes ratios based on disk galaxies in the HAGN simulation. Grey histograms show measurements in the simulation with 1σ errors displayed as black bars for each bin. Black solid lines show the fits to a truncated normal distribution, which are also shown as solid lines in the top panel of Fig. 11. Red dashed lines show the distribution reconstructed from fits to the the 2D axes ratio distribution which was derived from the 3D axes ratios using the ellipsoidal galaxy model (see central panel of Fig. 12). Dashed-dotted blue lines show the reconstruction based on fits to the 2D axes ratios measured from the projected stellar mass (see top panel of Fig. 12). Thin lines show predictions for 500 random sampling points of the posterior distributions and reflect the uncertainties expected on the prediction.

We emphasize that the conclusion drawn in this section could change when conducting these tests under more realistic conditions. An ideal test would be based on synthetic images including effects of dust extinction, lensing, PSF convolution and pixelization, as well as image noise. These images would then need to be analysed using the same software as used for the observations. Such a realistic test is beyond the scope of this work, but would be an interesting objective for future investigations.

	model	q_0	σ_q	γ_q	r_0	σ_r	γ_r
3D fits	skew Gauss	0.977	0.081	−5.009	0.426	0.112	2.016
3D fits	Gauss	0.921	0.049	-	0.504	0.073	-
2D rec. (proj. ellipsoids)	Gauss	0.934 [1.3, −4.4]	0.093 [−92.2]	-	0.515 [2.1, 20.9]	0.071 [−2.0]	-
2D rec. (proj. stellar mass)	Gauss	0.949 [3.0, −2.9]	0.017 [64.1]	-	0.464 [−8.0, 9.0]	0.062 [−14.6]	-

Table 3. Best fit parameters of the model for the 3D axis ratio distribution, derived for disk galaxies in the HAGN simulation at $z = 1.0$. The two top rows show results for the Gaussian and the skew Gaussian model from direct fits to the marginalised distributions of q_{3D} and r_{3D} (see Section 3.1), shown in Fig. 11. The two bottom rows show the parameters of the Gaussian model inferred from the distribution of 2D axis ratios using the reconstruction method. The 2D axis ratios used for the reconstruction are obtained either analytically from the galaxies 3D shapes, assuming that the stellar mass distributions are perfect 3D ellipsoids, or directly from shape measurements of the projected stellar mass distribution (labelled as projected ellipsoids and projected stellar mass respectively, see 12). The relative deviations of the reconstructed parameters with respect to those from the direct 3D fits are given in % in square brackets. For q_0 and r_0 we provide deviations from 3D fits to the Gaussian and skew Gaussian model as the first and second value respectively. For σ_q and σ_r we only provide deviations with respect to the Gaussian model.

stellar mass range	redshift range	N_{gal}	q_0	σ_q	r_0	σ_r	s_0	$\chi^2/d.o.f.$
$M_\star < 10^{10.35} M_\odot$	$0.2 < z < 1.0$	1913	$0.873^{0.895}_{0.864}$	$0.072^{0.1}_{0.06}$	$0.37^{0.385}_{0.357}$	$0.207^{0.232}_{0.195}$	$0.325^{0.339}_{0.314}$	1.282
	$0.2 < z < 0.7$	441	$0.889^{0.911}_{0.819}$	$0.051^{0.224}_{0.039}$	$0.427^{0.631}_{0.407}$	$0.207^{0.286}_{0.184}$	$0.377^{0.526}_{0.362}$	0.577
	$0.7 < z < 0.9$	785	$0.86^{0.884}_{0.841}$	$0.073^{0.114}_{0.056}$	$0.276^{0.314}_{0.112}$	$0.348^{0.522}_{0.295}$	$0.234^{0.273}_{0.095}$	0.982
	$0.9 < z < 1.0$	681	$0.833^{0.864}_{0.8}$	$0.064^{0.213}_{0.051}$	$0.353^{0.464}_{0.331}$	$0.201^{0.287}_{0.178}$	$0.295^{0.395}_{0.278}$	1.134
$M_\star > 10^{10.35} M_\odot$	$0.2 < z < 1.0$	1836	$0.906^{0.973}_{0.888}$	$0.147^{0.18}_{0.116}$	$0.257^{0.265}_{0.25}$	$0.055^{0.06}_{0.05}$	$0.24^{0.252}_{0.227}$	1.388
	$0.2 < z < 0.7$	530	$0.88^{0.939}_{0.862}$	$0.072^{0.148}_{0.055}$	$0.244^{0.257}_{0.235}$	$0.042^{0.055}_{0.032}$	$0.214^{0.234}_{0.208}$	0.793
	$0.7 < z < 0.9$	766	$0.983^{0.979}_{0.88}$	$0.254^{0.292}_{0.206}$	$0.271^{0.29}_{0.259}$	$0.055^{0.068}_{0.042}$	$0.256^{0.275}_{0.236}$	1.175
	$0.9 < z < 1.0$	536	$0.919^{0.972}_{0.882}$	$0.119^{0.154}_{0.082}$	$0.281^{0.298}_{0.268}$	$0.088^{0.105}_{0.072}$	$0.259^{0.28}_{0.245}$	0.874

Table 4. Parameters of model for the 3D axes ratio distribution (equation (5) and (6)), inferred from fits to the 2D axis ratio distribution, shown in Fig. 15. Results are shown for the six redshift-stellar mass samples and two mass samples defined over the full redshift range, as indicated in the left columns. For each model parameter we provide the lower and upper limit of the 68% confidence level, obtained from the marginalized posteriors. The distributions of the 3D axis ratios, predicted for COSMOS based on these parameters, are shown in Fig. 17.

4 3D AXES RATIO DISTRIBUTIONS IN COSMOS

We apply the method for reconstructing 3D axes ratio distributions to the two mass samples and the six stellar mass-redshift samples from the COSMOS observations, described in Section 2.1.6. The fits to the observed of 2D axes ratios from which we infer the parameters of our model for the 3D axes ratio distribution, are shown in Fig. 15. We find that the fits match the measurements well with χ^2 values per degree of freedom around unity (see Table 4), capturing the skewness towards low and high values of q_{2D} for the high and low mass samples, respectively (as shown in Fig. 9). Interestingly, the fits for the redshift sub-samples, (red solid lines in Fig. 15) are close to those for the entire redshift range (blue dashed lines). Thus, the redshift evolution of the axes ratio distribution in our samples is weak, if present at all, as we discuss in more detail below. We also note that these fits are better than those to the 2D axes ratio distributions from the projected stellar mass in the HAGN simulation, shown in the top panel of Fig. 12. This finding might result from the fact that we selected all disk galaxies in HAGN, including those with large bulges for which a one-component model is clearly an inadequate approximation. Additional reasons may be differences between the 2D shapes of the projected stellar mass and the projected luminosity densities or shortcomings of the simulation, caused for instance by resolution effects.

In Fig. 16 we show the MCMC estimates for the posterior probability distribution of the $P(q_{3D}, r_{3D})$ model parameters, q_0, r_0, σ_q and σ_r, quantifying the disk circularity, the relative disk thickness and the corresponding dispersions, respectively. The best fit parameters, defined as the positions of the maxima of the posteriors are summarized in Table 4. In this table we also provide results on the for the parameter $s_0 \equiv q_0 r_0$, whose posterior distribution we obtain directly from the sampling points of the posterior distributions of q_0 and r_0. It specifies the position of the maximum in the $P(q_{3D}, s_{3D})$ distribution and quantifies the disk thickness relative to the major axis, facilitating a comparison to the disk circularity parameter q_0.

The top sub-figure of Fig. 16 compares results from galaxies from the low and high mass sample in the entire redshift range. Overall we find q_0 values of around 0.9 for both samples, which is consistent with estimates reported for disks at lower redshifts in previous studies (Fasano et al. 1993; Ryden 2004, 2006; Rodríguez & Padilla 2013) and describes the deficit of circular face-on disks with $q_{2D} = 1.0$ in the observed data (see Fig. 15). Different reasons for this deficit have been discussed in the literature (e.g. Bertola et al. 1991; Huizinga & van Albada 1992; Rix & Zaritsky 1995; Bernstein & Jarvis 2002; Joachimi et al. 2013). On the one hand, it is argued that deviations from perfect circularity could result from observational effects, such as noisy isophotes, artifacts like cosmic rays in the galaxy images, or simply the fact that the images are pixelised. However, we expect the impact of such effects on our measurements to be minor, since i) we selected objects with "good" fits to the Sérsic profile (see Section 2.1.2), which should remove objects whose images are heavily distorted by artefacts from the sample and ii) the ACS pixel scale of 0.03" is well below our lowest limit for the effective angular radius of 0.17" at $z = 1.0$ (see Fig. 2). However, since the deviations from perfect circularity are predicted to be relatively small, even minor systematics might affect our conclusions regarding a physical origin of the non-circularity. On the other hand, one could expect that the disk galaxies are intrinsically not perfectly circular due to patchy star formation activity and substructures, such as spiral arms (see Fig. 1) or galactic warps (see e.g.

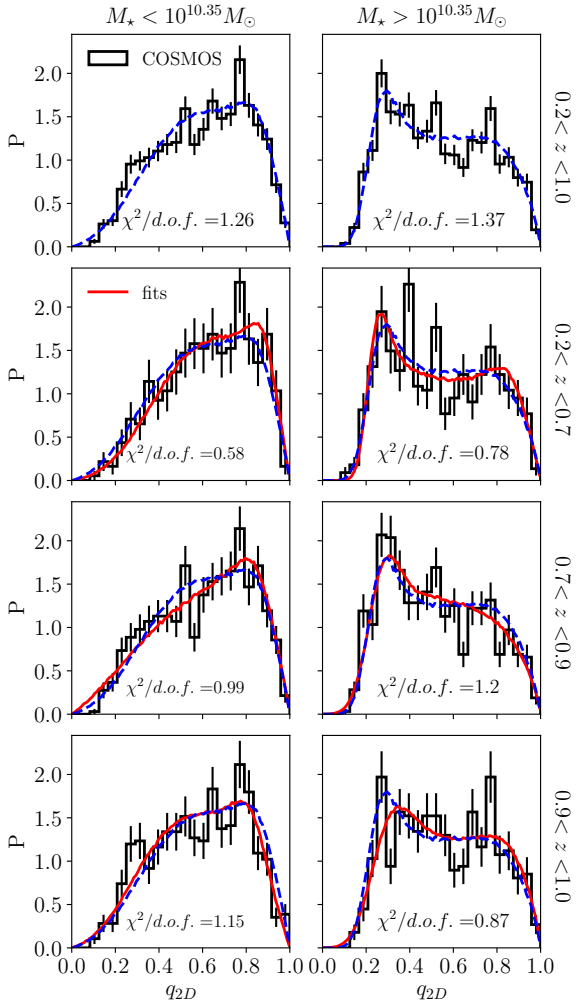

Figure 15. Probability distribution of apparent axes ratios q_{2D} of disks in the COSMOS survey with stellar masses below and above $10^{10.35} M_\odot$, shown as black histograms in the left and right panels respectively. Error bars show shot noise estimates of the standard deviation in each bin. Red lines show model predictions for the best fit parameters obtained from the posterior distribution shown in Fig. 16, which are summarized in Table 4.

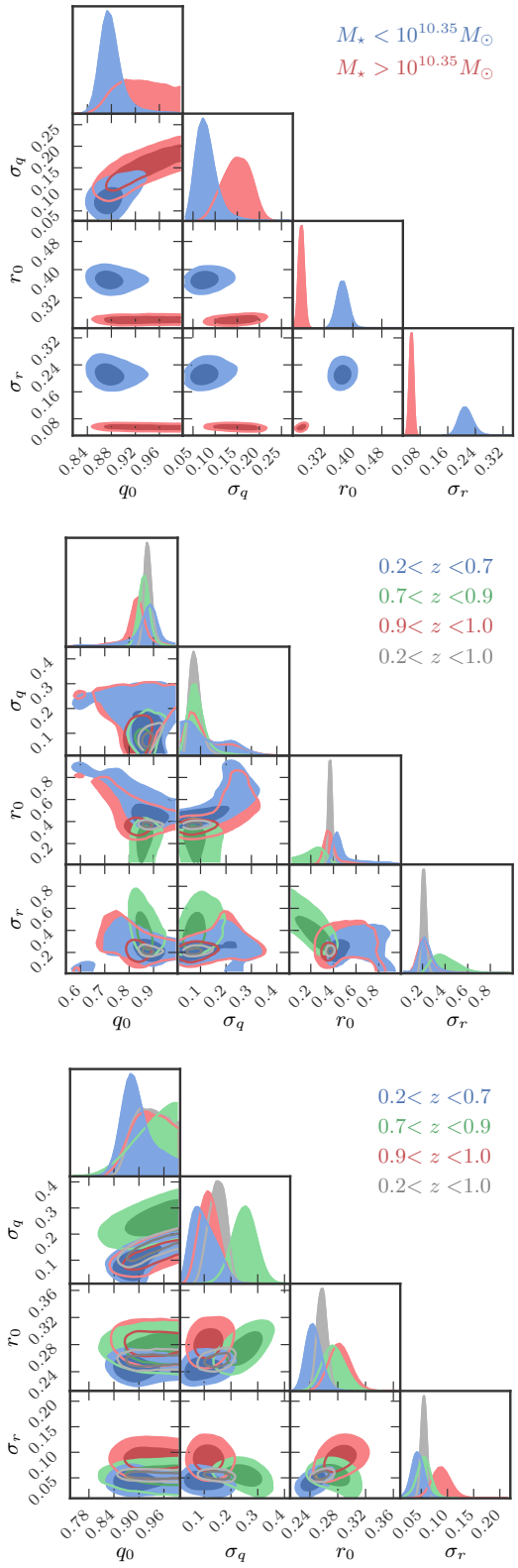

Figure 16. MCMC estimates of the posterior of the 3D axes ratio model parameters from equation (5), derived from the 2D axes ratio distributions in COSMOS (Fig. 15). Light and dark areas mark 95 and 68 % confidence levels respectively. The top figure shows results for low and high mass galaxies in the entire redshift range ($0.2 < z < 1.0$). The central and bottom figures compare results from galaxies in different redshift bins for the low and high mass samples respectively. The marginalized posterior distributions are shown on the diagonal panels of each figure.

Binney 1992; Gómez et al. 2017, for the latter). This expectation lines up with the non-circularity of disks in the HAGN and TNG100 simulations, which we see in Fig 11 and 12 as the lack of galaxies with q_{3D} and q_{2D} close to unity. We find in the top sub-figure of Fig. 16 that the high mass sample prefers slightly higher values of q_0 (i.e. higher circularity) compared to the low mass samples, although this mass dependence lies within the 2σ uncertainties. In contrast to q_0, we find a significant mass dependence of its dispersion, σ_q. The lower dispersion for low mass galaxies explains the sharper cut-off on the right side of the q_{2D} distribution, compared to the distribution of the high mass sample, which we see in Fig. 15. However, we expect this latter parameter to be biased by $\lesssim 70\%$

from our systematic tests based on the HAGN simulation (see Table 3).

The parameter r_0, which quantifies the maximum of the relative disk thickness distribution, defined as the minor to intermediate axes ratio, is predicted to be around 0.3 with lower and higher values for the high and low mass sample, respectively. The corresponding constraints on the relative thickness $s_0 \equiv q_0 r_0$ are 0.32 for the low mass and 0.24 for the high mass samples respectively. These latter values are consistent with results reported for disks at low redshifts which were obtained using the same reconstruction technique (Fasano et al. 1993; Ryden 2004, 2006; Rodríguez & Padilla 2013) or from direct measurements based on edge-on oriented disks (Mosenkov et al. 2015; Reshetnikov et al. 2016; Mosenkov et al. 2020). The dispersion of the relative disk thickness, σ_r, shows a significant mass dependence as well, as it takes lower and higher values for the high and low mass sample respectively. This mass dependence of the thickness dispersion explains why the cuff-off on the left side of the q_{2D} distribution in Fig. 15 is sharper for high than for low mass disks, while we expect also this latter parameter to be significantly biased by $\lesssim 20\%$ (Table 3).

The posterior probability distribution of the q_{3D} model parameters, estimated in low and high mass samples of the entire redshift range are compared to those from the corresponding redshift subsamples in the central and bottom of Fig. 16, respectively. Overall, we find no significant deviation between the posteriors from the low mass sample at different redshifts as the 68% confidence levels overlap plainly. For the high mass sample, we find stronger deviations, although the 95% confidence levels from all redshifts still overlap. The insignificant redshift dependence of the parameters does not necessarily mean that the shapes of disk dominated galaxies do not evolve since $z = 1.0$, but indicates that a potential evolution is too weak to be detected given the errors which we estimate for the samples in our analysis.

In Fig. 17 we show the reconstructed marginalized distributions of the 3D axes ratios q_{3D} and r_{3D} for the low and high mass sample over the full redshift range, as predicted from the best fit parameters. The uncertainties on the prediction are shown as thin lines, obtained from random-sampling the posterior. The corresponding values q_0 and r_0 are shown as vertical lines. They are enclosed by shaded areas which indicate the bias of 3% and 9% respectively, which we found for these parameters from our systematic tests (Table 3). When comparing the distributions of both mass samples, we see that the values of r_{3D} are well below those of q_{3D} as expected for disk galaxies. This indicates that our results carry physically meaningful information, despite the expected bias on the absolute values. Fig. 17 further illustrates that i) high mass disks tend to be thinner with respect to their diameter than low mass disks, ii) high mass disks tend to be slightly more circular than low mass disks and iii) the dispersion of the circularity and the relative thickness is larger for low mass than for high mass disks. However, the figure shows that the mass dependence of the circularity q_0 is within the expected systematic uncertainty, as the shaded areas in the top panel strongly overlap. Since we also expect the dispersions of the distributions to be significantly biased, we focus our discussion on the relative disk thickness. The lower relative thickness for high mass disks could indicate that these galaxies tend to be more relaxed than low mass disks, which are more prone to perturbations by feedback, merging and tidal interactions. This interpretation is supported by the higher dispersion of the relative thickness of low mass disks and lines up with the overall higher star formation rates for low mass disks, which we see in Figure 9. However, another reason to expect a lower relative thickness of massive disks with respect to their

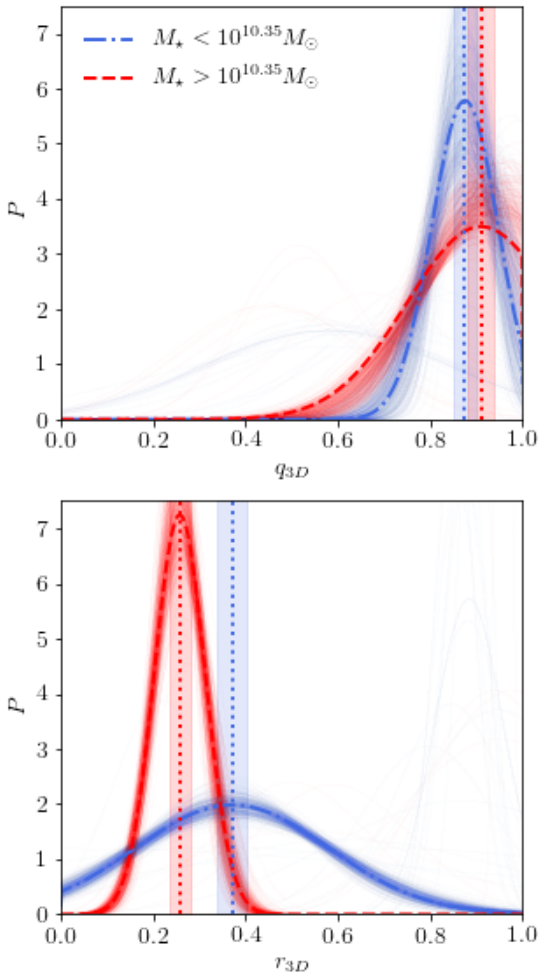

Figure 17. Marginalized distributions of 3D axes ratios reconstructed from the 2D axes ratio distribution in the COSMOS survey. Results are shown for the low and high mass sample, defined with $0.2 < z < 1.0$. Horizontal lines mark the positions of the maxima, described by the model parameters q_0 and r_0. Horizontal shaded areas indicate 3 and 9 % uncertainties on q_0 and r_0 respectively, which correspond to the bias which we expect from testing reconstruction method using the shapes of projected stellar mass distributions in HAGN (see Table 3). Thin lines show predictions for 500 random sampling points of the posterior distribution.

major axes is that the latter is on average larger for disks in the high mass sample (see Fig. 9). In order to test this latter hypothesis we derive an estimate of the expected absolute thickness $\langle C_{3D} \rangle$ from the reconstructed s_{3D} axes ratios and the absolute comoving size of the major axis A_{3D}. We approximate the expectation value of s_{3D} for a given galaxy sample with the best fit parameter for s_0. The expectation value for A_{3D} is estimated to be the mean effective comoving radius, measured for galaxies in the same sample, using objects with $q_{2D} > 0.5$, as shown in Fig. 9. In the top panel of Fig. 18, we show the posterior probability distributions of s_0 derived from the low mass and high mass sample in the entire redshift range. Both posteriors differ significantly from each other, as it can be expected from the constraints on r_0 (Fig. 16). In the bottom panel of Fig. 18, we show estimates for the posterior of the expected 3D minor axis sizes $\langle C_{3D} \rangle$ for both samples. The two posteriors overlap each other almost completely, which means that our approximation of the 3D disk thickness shows no significant mass dependence.

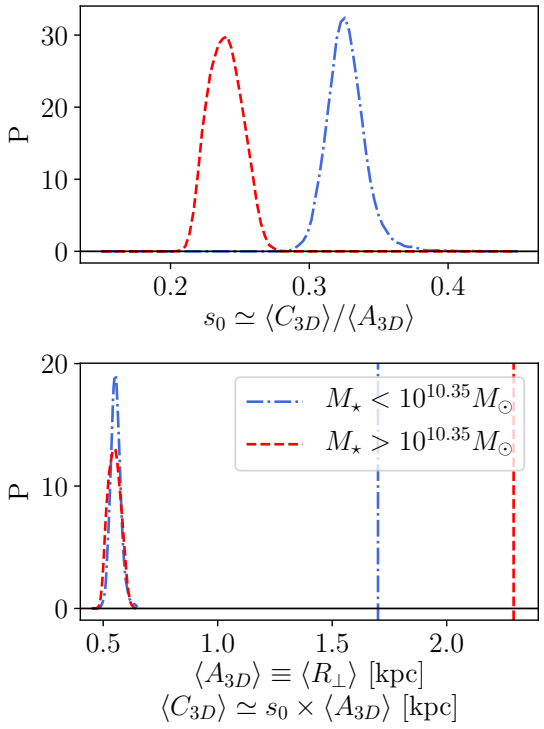

Figure 18. *Top*: MCMC estimate of the marginalized probability distribution for the parameter $s_0 \equiv q_0 r_0$. *Bottom*: Estimate of the probability distribution of the minor axes sizes, assuming that the major axes (marked as horizontal lines) correspond to the comoving effective radius, averaged over all disks with $q_{2D} > 0.5$.

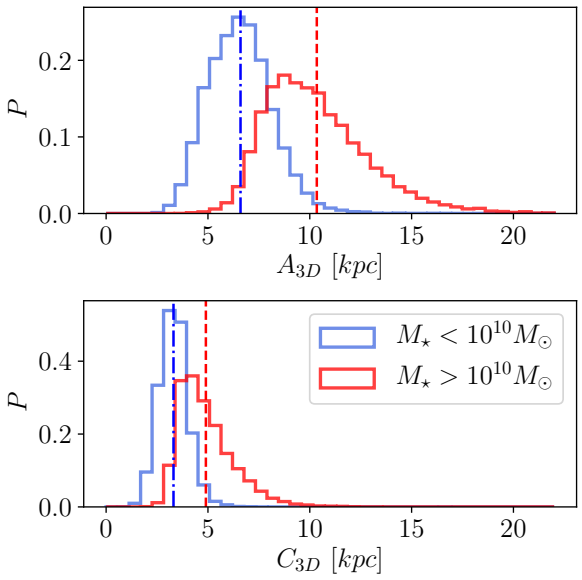

Figure 19. Distribution of minor and major axes sizes, obtained from the simple moment of inertia, for disk galaxies in the HAGN simulation at redshift $z = 1.0$. The axes are re-scaled, such that $(A_{3D} + B_{3D} + C_{3D})/3$ corresponds to the half mass radius. Results are shown for disks with stellar masses higher and lower than $10^{10} M_\odot$, which is slightly above the median stellar mass of $0.74\ 10^{10} M_\odot$. Horizontal lines, mark the mean value for each distribution. The figure shows that the absolute sizes of the principle axes increase with mass and that this increase is stronger for the major than for the minor axes, which quantify the disk diameter and thickness respectively.

These posterior distributions are compared to the estimates of the mean major axes sizes $\langle A_{3D}\rangle$ which are shown as vertical lines in the same panel. The strong mass dependence, which we find for $\langle A_{3D}\rangle$ suggests that the mass dependence in the relative 3D thickness s_{3D} (Fig. 17) is mainly driven by the difference of the major axes sizes.

We validate this conclusion by comparing the distribution of the major and minor axes sizes of high and low mass disks in the HAGN simulation, which are selected as described in Section 2.2.1. The results, shown in Fig. 19, show that the absolute difference between the major axes sizes in the high and low mass samples is larger than the absolute difference between their minor axes sizes (top and bottom panel respectively). The mass dependence in the distribution of the relative thickness s_{3D} can hence be considered to be driven mainly by the mass dependence of the major axis, while the mass dependence of the minor axis size is relatively weak and could result from the fact that the HAGN sample includes disks with and without large bulges. This finding supports our conclusions drawn from the observed data. A more detailed comparison between simulations and observations would require a consistent sample selection and data analysis.

5 SUMMARY AND CONCLUSIONS

We studied the 3D shapes of disk dominated late type galaxies from the COSMOS survey in different mass and redshift ranges, tackling the question of how these galaxies could grow without forming a large central bulge. We approximated the 3D light distribution of these galaxies as 3D ellipsoids described by the two ratios $q_{3D} \equiv B_{3D}/A_{3D}$ and $r_{3D} \equiv C_{3D}/B_{3D}$, which quantify the circularity and relative thickness of the disks, respectively. We inferred the distribution of these 3D axes ratios from the observed distribution of 2D axes ratios, using a reconstruction method based on the assumption that the distribution of q_{3D} and r_{3D} is well approximated by a two-dimensional Gaussian.

Variations of this method have been widely used in the literature, but their accuracy as well as the assumptions they employ remained to be tested. We began our analysis by performing such tests for the first time using two state-of-the-art hydrodynamic simulations of galaxy formation in cosmological volumes, Horizon AGN and Illustris TNG100. We demonstrated that the 3D axes ratio distributions of disk galaxies in these simulations are adequately described by a Gaussian model. Reconstructing the 3D axes ratio distribution from the distribution of 2D axes ratios we found that the inferred parameters of the Gaussian model are biased with respect to those derived directly from fits to the 3D distributions. For our most realistic test, based on 2D galaxy shapes from projected stellar mass distributions, we find this bias to be moderate for the parameters q_0 and r_0 ($\sim 3\%$ and $\sim 9\%$ respectively), which quantify the position of the maximum of the joint q_{3D}-r_{3D} distribution, but strong for the corresponding dispersions σ_q and σ_r ($\sim 65\%$ and $\sim 9\%$ respectively, see Table 3). We concluded that the bias is mainly driven by an inaccuracy of the ellipsoidal model for the stellar mass distribution, which we use for relating 3D to 2D galaxy shapes analytically during the reconstruction (see Section 3.3). The strong simplification implied when approximating late type galaxies as 3D ellipsoids becomes obvious in the COSMOS images of such objects, shown in Fig. 1. Nevertheless, our bias estimates derived

from the HAGN simulation may be overly pessimistic, since our test is based on all disk galaxies found in this simulation, including those which have a bulge for which a one-component ellipsoidal galaxy model is expected to be inadequate. More realistic tests should be based on synthetic galaxy images, take into account the effect of dust extinction and be analysed in the same way as the reference observational data.

After having tested the shape reconstruction method we applied it on a volume limited sample of disk dominated galaxies in COSMOS which is limited in redshift ($0.2 < z < 1.0$), absolute magnitude ($M_i < -21.5$) and transverse comoving size ($R_\perp > 0.64$ kpc). We demonstrated that a conservative cut on M_i is required in order to minimize the impact of dust extinction the observed 2D axes ratio distribution. Otherwise, this effect can lead to an apparent redshift evolution of the distribution (Fig. B1) and consequently to incorrect physical interpretations of the observations. We found that the ellipsoidal galaxy shape model in conjunction with the Gaussian model for the 3D axes ratio distribution provides good fits to the distribution of the observed 2D axis ratios (Fig. 15). The model parameters inferred from these fits showed no significant dependence on redshift, which is contrasted by a relatively strong dependence on mass (Fig. 16). In particular, the parameter r_0 is significantly higher for disks in our sample with stellar masses below $10^{10.35} M_\odot$ compared to disks with higher masses, even within the expected uncertainties of the reconstruction method (e.g. Fig. 17). This finding indicates that the relative disk thickness decreases with mass. However, the absolute disk thickness, estimated from the relative thickness and a proxy for the disk diameter, shows no mass dependence (Fig. 18), which suggests that the relative thickness of low mass disks is higher mainly because of their smaller diameters (e.g. Fig. 9).

In summary, we found indications that the distributions of the 3D axes ratios of disk dominated galaxies in our sample is not redshift dependent in the range $0.2 < z < 1.0$ and the absolute disk thickness does not depend on mass. These findings speak against mass accretion by major mergers and a subsequent suppression of bulge formation by strong feedback after $z \lesssim 1.0$, since one could expect that such disruptive events would decrease the disks circularity and increase their thickness due to to vertical heating (e.g. Quinn et al. 1993; et al. 2016; Park et al. 2020). The decrease of the specific star formation rates of massive disks with redshift, shown in Fig. 9, suggests that feedback occurs in these galaxies, suppressing star formation by removing cold gas, but may not be sufficiently strong to significantly affect the observed shapes. The absence of major mergers in disk dominated galaxies since $z \lesssim 1$ is further supported by the fact that the mean comoving sizes, displayed in Fig. 9, show no redshift evolution for low mass galaxies and a very weak increase with redshift for high mass galaxies. We conclude that disk-dominated galaxies accreted most of their mass before $z = 1.0$ and lived preferentially in isolation ever since. This picture lines up with the results from Grossi et al. (2018), who find that the star formation rates of disk-dominated galaxies show no significant dependence on the density of their environment, which indicates the absence of major interactions.

However, we emphasize that the validity of our results is limited for several reasons. The small sizes of our samples lead to large statistical errors, which may obscure a weak evolution of the galaxy shapes with redshift and could hence affect our conclusions. This limitation can be overcome in future analysis by using measurements of galaxy shapes in larger volumes from upcoming weak lensing surveys like *Euclid* or the Legacy Survey of Space and Time on the Vera Rubin Observatory. Such high precision measurements will require an improved accuracy of the shape reconstruction method, based for instance on corrections which can be developed using realistic mock images. More detailed interpretations of the redshift evolution of observed galaxy shapes may also require a characterization of two effects which we assumed to be insignificant with respect to the errors on our measurements. A first potential systematic in the observations could result from the fact that galaxy shapes are observed in the same filter at different redshifts. High redshift galaxies are therefore seen at bluer rest frame wavelengths than galaxies at lower redshifts. This may affect the observed shapes for two reasons. The first is that the age of stellar populations is not uniformly distributed, as star formation takes place in distinct regions such as spiral arms (e.g. Martin & Kennicutt 2001). The second reason is that extinction and reddening by dust in the source galaxy has a stronger impact on observations in blue than in red rest-frame wavelengths and may hence distort the observed shapes more strongly at high than at lower redshifts. The latter effects is further complicated by the fact that the distribution and overall density of dust evolves with time. In fact, we find strong indications of dust extinction in our data (Fig. B1). However, studying shapes measured from synthetic galaxy images, we find no strong dependence of the 2D axis ratio distribution on the filter band, which suggests that dust extinction has on average only a mild effect on the observed shapes (see Appendix B). A second systematic effect can be expected from gravitational lensing, while effect is typically weak with a contribution of less than 1% to the observed ellipticity (e.g. Kirk et al. 2015).

An important outcome of our analysis is that the model for the 3D galaxy shapes and their distribution provides good fits to the observed distribution of 2D shapes for disk dominated galaxies, despite the expected inaccuracies. This model can hence be employed to generate mock catalogs of galaxy shapes in large cosmological dark matter-only simulations in which stellar mass distributions of individual galaxies are not provided. In order to construct such mocks, Joachimi et al. (2013) approximated disk galaxies by flat opaque cylinders and showed that the resulting 2D ellipticity distribution differs significantly from COSMOS observations. An improvement on this aspect is crucial for building precision mock galaxy catalogs with intrinsic alignments for the preparation of future weak lensing surveys. Disk galaxies are expected to dominate the lensing source samples at high redshifts in which intrinsic alignments contaminate the gravitational shear induced by the large scale structure at lower redshifts (e.g. Fig. 5). Building and testing such improved mocks is subject of our ongoing work.

ACKNOWLEDGEMENTS

KH acknowledges support by the Swiss National Science Foundation (SNF CRSII5 173716). CL acknowledges support from the Programme National Cosmology and Galaxies (PNCG) of CNRS/INSU with INP and IN2P3. This work is part of the Delta ITP consortium, a program of the Netherlands Organisation for Scientific Research (NWO) that is funded by the Dutch Ministry of Education, Culture and Science (OCW). The research of JD is supported by the Beecroft Trust and STFC. We thank Romain Teyssier for fruitful discussions and comments on this paper. Our analysis is based on data products from observations made with ESO Telescopes at the LaSilla Paranal Observatory under ESO programme ID 179.A-2005 and on data products produced by TERAPIX and the Cambridge Astronomy Survey Unit on behalf of the UltraVISTA consortium. Our analysis was performed using Jupyter Notebook (Kluyver et al. 2016), with the Python packages Colossus (Diemer

2018), emcee (Foreman-Mackey et al. 2013), Matplotlib (Hunter 2007), NumPy (Harris et al. 2020), pandas (Wes McKinney 2010), pyGTC Bocquet & Carter (2016), SciPy (Virtanen et al. 2020).

References

R. J. J., Springel V., Gómez F. A., Marinacci F., Pakmor R., Campbell D. J. R., Jenkins A., 2016, MNRAS, 459, 199
Abadi M. G., Navarro J. F., Steinmetz M., Eke V. R., 2003, ApJ, 597, 21
Aguerri J. A. L., Balcells M., Peletier R. F., 2001, A&A, 367, 428
Aubert D., Pichon C., Colombi S., 2004, MNRAS, 352, 376
Baldry I. K., Glazebrook K., Brinkmann J., Ivezić Ž., Lupton R. H., Nichol R. C., Szalay A. S., 2004, ApJ, 600, 681
Baugh C. M., Cole S., Frenk C. S., 1996, MNRAS, 283, 1361
Benacchio L., Galletta G., 1980, MNRAS, 193, 885
Bernstein G. M., Jarvis M., 2002, AJ, 123, 583
Bertin E., Arnouts S., 1996, A&AS, 117, 393
Bertola F., Vietri M., Zeilinger W. W., 1991, ApJ, 374, L13
Bignone L. A., Pedrosa S. E., Trayford J. W., Tissera P. B., Pellizza L. J., 2020, MNRAS, 491, 3624
Binney J., 1978, MNRAS, 183, 501
Binney J., 1985, MNRAS, 212, 767
Binney J., 1992, ARA&A, 30, 51
Binney J., Tremaine S., 2008, Galactic Dynamics: Second Edition
Binney J., de Vaucouleurs G., 1981, MNRAS, 194, 679
Bocquet S., Carter F. W., 2016, The Journal of Open Source Software, 1
Bournaud F., 2016, Bulge Growth Through Disc Instabilities in High-Redshift Galaxies. p. 355, doi:10.1007/978-3-319-19378-6_13
Brook C. B., et al., 2011, MNRAS, 415, 1051
Brook C. B., Stinson G., Gibson B. K., Roškar R., Wadsley J., Quinn T., 2012, MNRAS, 419, 771
Brooks A., Christensen C., 2016, Bulge Formation via Mergers in Cosmological Simulations. p. 317, doi:10.1007/978-3-319-19378-6_12
Bundy K., et al., 2010, ApJ, 719, 1969
Buta R. J., et al., 2015, ApJS, 217, 32
Carollo D., et al., 2010, ApJ, 712, 692
Chang Y.-Y., et al., 2013, ApJ, 773, 149
Chisari N., et al., 2015, MNRAS, 454, 2736
Correa C. A., Schaye J., Clauwens B., Bower R. G., Crain R. A., Schaller M., Theuns T., Thob A. C. R., 2017, MNRAS, 472, L45
Davis M., Efstathiou G., Frenk C. S., White S. D. M., 1985, ApJ, 292, 371
Debattista V. P., Mayer L., Carollo C. M., Moore B., Wadsley J., Quinn T., 2006, ApJ, 645, 209
Diemer B., 2018, ApJS, 239, 35
Dolag K., Borgani S., Murante G., Springel V., 2009, MNRAS, 399, 497
Dubois Y., Pichon C., Haehnelt M., Kimm T., Slyz A., Devriendt J., Pogosyan D., 2012, MNRAS, 423, 3616
Dubois Y., et al., 2014, MNRAS, 444, 1453
Dubois Y., Peirani S., Pichon C., Devriendt J., Gavazzi R., Welker C., Volonteri M., 2016, MNRAS, 463, 3948
Eliche-Moral M. C., Balcells M., Aguerri J. A. L., González-García A. C., 2006, A&A, 457, 91
Elmegreen B. G., Bournaud F., Elmegreen D. M., 2008, ApJ, 688, 67
Fasano G., Amico P., Bertola F., Vio R., Zeilinger W. W., 1993, MNRAS, 262, 109
Foreman-Mackey D., Hogg D. W., Lang D., Goodman J., 2013, PASP, 125, 306
Genel S., Fall S. M., Hernquist L., Vogelsberger M., Snyder G. F., Rodriguez-Gomez V., Sijacki D., Springel V., 2015, ApJ, 804, L40
Georgiou C., et al., 2019, A&A, 622, A90
Gómez F. A., White S. D. M., Grand R. J. J., Marinacci F., Springel V., Pakmor R., 2017, MNRAS, 465, 3446
Governato F., et al., 2010, Nature, 463, 203
Grand R. J. J., et al., 2017, MNRAS, 467, 179
Griffith R. L., et al., 2012, ApJS, 200, 9
Grossi M., Fernandes C. A. C., Sobral D., Afonso J., Telles E., Bizzocchi L., Paulino-Afonso A., Matute I., 2018, MNRAS, 475, 735
Guo R., Hao C.-N., Xia X., Shi Y., Chen Y., Li S., Gu Q., 2020, ApJ, 897, 162
Harris C. R., et al., 2020, Nature, 585, 357
Hatfield P. W., Laigle C., Jarvis M. J., Devriendt J., Davidzon I., Ilbert O., Pichon C., Dubois Y., 2019, MNRAS, 490, 5043
Häußler B., Barden M., Bamford S. P., Rojas A., 2011, in Evans I. N., Accomazzi A., Mink D. J., Rots A. H., eds, Astronomical Society of the Pacific Conference Series Vol. 442, Astronomical Data Analysis Software and Systems XX. p. 155
Heidmann J., Heidmann N., de Vaucouleurs G., 1972, Mem. RAS, 75, 121
Hoffmann K., et al., 2014, MNRAS, 442, 1197
Holden B. P., van der Wel A., Rix H.-W., Franx M., 2012, ApJ, 749, 96
Holmberg E., 1946, Meddelanden fran Lunds Astronomiska Observatorium Serie II, 117, 3
Hopkins P. F., Cox T. J., Younger J. D., Hernquist L., 2009, ApJ, 691, 1168
Hopkins P. F., Kereš D., Murray N., Quataert E., Hernquist L., 2012, MNRAS, 427, 968
Hubble E. P., 1926, ApJ, 64, 321
Huizinga J. E., van Albada T. S., 1992, MNRAS, 254, 677
Hunter J. D., 2007, Computing in Science & Engineering, 9, 90
Ilbert O., et al., 2006, A&A, 457, 841
Joachimi B., Semboloni E., Bett P. E., Hartlap J., Hilbert S., Hoekstra H., Schneider P., Schrabback T., 2013, MNRAS, 431, 477
Kauffmann G., White S. D. M., Guiderdoni B., 1993, MNRAS, 264, 201
Kautsch S. J., 2009, PASP, 121, 1297
Kautsch S. J., Grebel E. K., Barazza F. D., Gallagher J. S. I., 2006, A&A, 445, 765
Kaviraj S., et al., 2017, MNRAS, 467, 4739
Kepner J. V., 1999, ApJ, 520, 59
Kirk D., et al., 2015, Space Sci. Rev., 193, 139
Kluyver T., et al., 2016, in Loizides F., Schmidt B., eds, Positioning and Power in Academic Publishing: Players, Agents and Agendas. pp 87 – 90
Komatsu E., et al., 2011, ApJS, 192, 18
Kormendy J., 2016, Elliptical Galaxies and Bulges of Disc Galaxies: Summary of Progress and Outstanding Issues. p. 431, doi:10.1007/978-3-319-19378-6_16
Kormendy J., Kennicutt Robert C. J., 2004, ARA&A, 42, 603
Kormendy J., Drory N., Bender R., Cornell M. E., 2010, ApJ, 723, 54
Kretschmer M., Agertz O., Teyssier R., 2020, MNRAS, 497, 4346
Laigle C., et al., 2016, ApJS, 224, 24
Laigle C., et al., 2019, MNRAS, 486, 5104
Lambas D. G., Maddox S. J., Loveday J., 1992, MNRAS, 258, 404
Larson R. B., Tinsley B. M., Caldwell C. N., 1980, ApJ, 237, 692
Lilly S. J., et al., 2007, ApJS, 172, 70
Marinacci F., et al., 2018, MNRAS, 480, 5113
Martig M., Bournaud F., Teyssier R., Dekel A., 2009, ApJ, 707, 250
Martin C. L., Kennicutt Robert C. J., 2001, ApJ, 555, 301
Martínez-Lombilla C., Knapen J. H., 2019, A&A, 629, A12
Mosenkov A. V., Sotnikova N. Y., Reshetnikov V. P., Bizyaev D. V., Kautsch S. J., 2015, MNRAS, 451, 2376
Mosenkov A., et al., 2020, MNRAS, 494, 1751
Naiman J. P., et al., 2018, MNRAS, 477, 1206
Nelson D., et al., 2018, MNRAS, 475, 624
Noerdlinger P. D., 1979, ApJ, 234, 802
Padilla N. D., Strauss M. A., 2008, MNRAS, 388, 1321
Park M.-J., et al., 2019, ApJ, 883, 25
Park M. J., et al., 2020, arXiv e-prints, p. arXiv:2009.12373
Peebles P. J. E., 2020, MNRAS, 498, 4386
Peng C. Y., Ho L. C., Impey C. D., Rix H.-W., 2002, AJ, 124, 266
Pillepich A., et al., 2018a, MNRAS, 473, 4077
Pillepich A., et al., 2018b, MNRAS, 475, 648
Pillepich A., et al., 2019, MNRAS, 490, 3196
Planck Collaboration et al., 2016, A&A, 594, A13
Planck Collaboration et al., 2018, arXiv e-prints, p. arXiv:1807.06209
Quinn P. J., Hernquist L., Fullagar D. P., 1993, ApJ, 403, 74
Reshetnikov V. P., Mosenkov A. V., Moiseev A. V., Kotov S. S., Savchenko S. S., 2016, MNRAS, 461, 4233

Rix H.-W., Zaritsky D., 1995, ApJ, 447, 82
Rodríguez S., Padilla N. D., 2013, MNRAS, 434, 2153
Rodriguez-Gomez V., et al., 2019, MNRAS, 483, 4140
Ryden B. S., 2004, ApJ, 601, 214
Ryden B. S., 2006, ApJ, 641, 773
Sachdeva S., 2013, MNRAS, 435, 1186
Sandage A., Freeman K. C., Stokes N. R., 1970, ApJ, 160, 831
Sargent M. T., et al., 2007, ApJS, 172, 434
Satoh Y. K., Kajisawa M., Himoto K. G., 2019, arXiv e-prints, p. arXiv:1909.08550
Scarlata C., et al., 2006, arXiv e-prints, pp astro–ph/0611644
Scarlata C., et al., 2007, ApJS, 172, 494
Scoville N., et al., 2007, ApJS, 172, 1
Snyder G. F., et al., 2015, MNRAS, 454, 1886
Springel V., 2010, MNRAS, 401, 791
Springel V., White S. D. M., Tormen G., Kauffmann G., 2001, MNRAS, 328, 726
Springel V., et al., 2018, MNRAS, 475, 676
Stark A. A., 1977, ApJ, 213, 368
Strateva I., et al., 2001, AJ, 122, 1861
Tacchella S., et al., 2019, MNRAS, 487, 5416
Takeuchi T. M., Ohta K., Yuma S., Yabe K., 2015, ApJ, 801, 2
Teyssier R., 2002, A&A, 385, 337
Trujillo I., Bakos J., 2013, MNRAS, 431, 1121
Übler H., Naab T., Oser L., Aumer M., Sales L. V., White S. D. M., 2014, MNRAS, 443, 2092
Vincent R. A., Ryden B. S., 2005, ApJ, 623, 137
Virtanen P., et al., 2020, Nature Methods, 17, 261
Vogelsberger M., et al., 2014, MNRAS, 444, 1518
Vogelsberger M., Marinacci F., Torrey P., Puchwein E., 2020, Nature Reviews Physics, 2, 42
Walker I. R., Mihos J. C., Hernquist L., 1996, ApJ, 460, 121
Weinzirl T., Jogee S., Khochfar S., Burkert A., Kormendy J., 2009, ApJ, 696, 411
Wes McKinney 2010, in Stéfan van der Walt Jarrod Millman eds, Proceedings of the 9th Python in Science Conference. pp 56 – 61, doi:10.25080/Majora-92bf1922-00a
Yuma S., Ohta K., Yabe K., Kajisawa M., Ichikawa T., 2011, ApJ, 736, 92
Yuma S., Ohta K., Yabe K., 2012, ApJ, 761, 19
Zhang H., et al., 2019, MNRAS, 484, 5170
de Vaucouleurs G., 1959, AJ, 64, 397
van den Bosch F. C., 1998, ApJ, 507, 601
van der Wel A., et al., 2014, ApJ, 792, L6

APPENDIX A: FROM 3D TO 2D AXES RATIOS

We obtain the 2D axis ratios of a projected 3D ellipsoidal stellar system following Joachimi et al. (2013), under the assumption that the 3D system is absorption-free, self-similar and coaxial. A 3D ellipsoid is thereby expressed in a coordinate system defined by the two orthogonal unit vectors $\{\hat{\boldsymbol{e}}_u, \hat{\boldsymbol{e}}_v\}$ which span the projection plane and the unit vector $\hat{\boldsymbol{e}}_{\parallel}$, which is orthogonal to $\{\hat{\boldsymbol{e}}_u, \hat{\boldsymbol{e}}_v\}$, pointing along the observer's line of sight. In this new coordinate system the principal axes are given by $\tilde{\mathbf{S}}_\mu = \{\langle\hat{\boldsymbol{e}}_u \boldsymbol{S}_\mu\rangle, \langle\hat{\boldsymbol{e}}_v \boldsymbol{S}_\mu\rangle, \langle\hat{\boldsymbol{e}}_\parallel \boldsymbol{S}_\mu\rangle\}^\tau \equiv \{\tilde{S}_{u,\mu}, \tilde{S}_{v,\mu}, \tilde{S}_{\parallel,\mu}\}^\tau$ with $\mathbf{S}_\mu \in \{\boldsymbol{A}_{3D}, \boldsymbol{B}_{3D}, \boldsymbol{C}_{3D}\}$. The projected 2D ellipse is given by all points $\boldsymbol{r}$ in the projection plane which fulfil $\boldsymbol{r}^\tau \mathbf{W}^{-1} \boldsymbol{r} = 1$, where

$$\mathbf{W}^{-1} \equiv \sum_{\mu=1}^{3} \frac{\tilde{\mathbf{S}}_{\perp,\mu} \tilde{\mathbf{S}}_{\perp,\mu}^\tau}{\tilde{S}_\mu^2} - \frac{\boldsymbol{k}\boldsymbol{k}^\tau}{\alpha^2}\,, \tag{A1}$$

with

$$\boldsymbol{k} \equiv \sum_{\mu=1}^{3} \frac{\tilde{S}_{\parallel,\mu} \tilde{\boldsymbol{S}}_{\perp,\mu}}{\tilde{S}_\mu^2} \quad \text{and} \quad \alpha^2 \equiv \sum_{\mu=1}^{3} \left(\frac{\tilde{S}_{\parallel,\mu}}{\tilde{S}_\mu}\right)^2\,, \tag{A2}$$

where $\tilde{\boldsymbol{S}}_{\perp,\mu} \equiv \{\tilde{S}_{u,\mu}, \tilde{S}_{v,\mu}\}^\tau$ is the principal axes component in the projection plane. The 2D ellipticity vector of the projected ellipsoid is then given by

$$\begin{pmatrix}\epsilon_1 \\ \epsilon_2\end{pmatrix} = \frac{1}{\mathcal{N}} \begin{pmatrix}W_{11} - W_{22} \\ 2\,W_{12}\end{pmatrix} \tag{A3}$$

with $\mathcal{N} \equiv W_{11} + W_{22} + \sqrt{\det \mathbf{W}}$. The absolute value of the ellipticity, $\epsilon = \sqrt{\epsilon_1^2 + \epsilon_2^2}$, is related to the 2D axis ratio $q_{2D} \equiv B_{2D}/A_{2D}$ of the projected ellipsoid as

$$q_{2D} = \frac{1-\epsilon}{1+\epsilon}, \tag{A4}$$

where A_{2D} and B_{2D} are the principle axes of the 2D ellipse. An alternative approach for obtaining q_{2D} has been derived by Binney (1985) (see also Stark 1977; Benacchio & Galletta 1980). However, we find this latter calculation to be computationally less efficient.

A1 Validating the model for the 3D axes ratio distribution

We use the shapes of disk galaxies, measured in the HAGN and TNG100 simulations to further validate assumptions of our model for the 3D axes ratio distribution, introduced in Section 3.1. The first assumption is that the 3D axes ratios $r_{3D} \equiv C_{3D}/A_{3D}$ and $r_{3D} \equiv C_{3D}/A_{3D}$ are uncorrelated. In Fig. A1 we compare kernel density estimates of the 3D axes ratio distribution from both simulations with those from sample points, drawn from our Gaussian model from equation (5). The model parameters are obtained from the fits to the marginalized 3D axes ratio distributions, shown in Fig. 11. We find that the model describes the simulation data reasonably well, although a weak correlation between q_{3D} and r_{3D} is clearly present. A possible improvement of the Gaussian model for the 3D axes ratio distribution could be the inclusion of a skewness in the q_{3D} dimension, as demonstrated in Fig. 11. In the top panel of Fig. A2, we show the joint distribution of q_{3D} and r_{3D} for the truncated Gaussian model with and without skewness, using parameters which are typical for the disk galaxies in our analysis. The corresponding distribution of the apparent 2D axes ratios are shown in the bottom panel of the same figure. We find that the effect of the skewness is small compared to the errors on our measurements (see Fig. 15). As a consequence the skewness in the q_{3D} distribution cannot be constrained from our observed data and is therefore not included in our $P(q_{3D}, r_{3D})$ model.

APPENDIX B: BIAS IN THE 2D AXES RATIO DISTRIBUTIONS FROM APPARENT MAGNITUDE CUTS

We study the effect of dust extinction on the $i - j$ color index and apparent i-band magnitude of the disk dominated galaxies in our volume limited sample by displaying these properties against the apparent 2D axis ratio q_{2D} in Fig. B1. For disky objects we expect q_{2D} to be tightly correlated with the objects inclination angle with respect to the observer and hence with the amplitude of the extinction. Dust extinction is expected to redden the observed spectra. This effect becomes apparent in the top panel of Fig. B1 as the color index increases with decreasing axes ratios, indicating an increased reddening of the spectra as the disks are inclined towards edge-on orientations. This effect can be expected from the increased path length which the light has to travel though the galactic medium of edge-on disks. The correlation between color-index and q_{2D} is tighter at lower redshifts, which speaks for an increase of dust extinction as galaxies evolve. The reddening of galaxy colors by dust

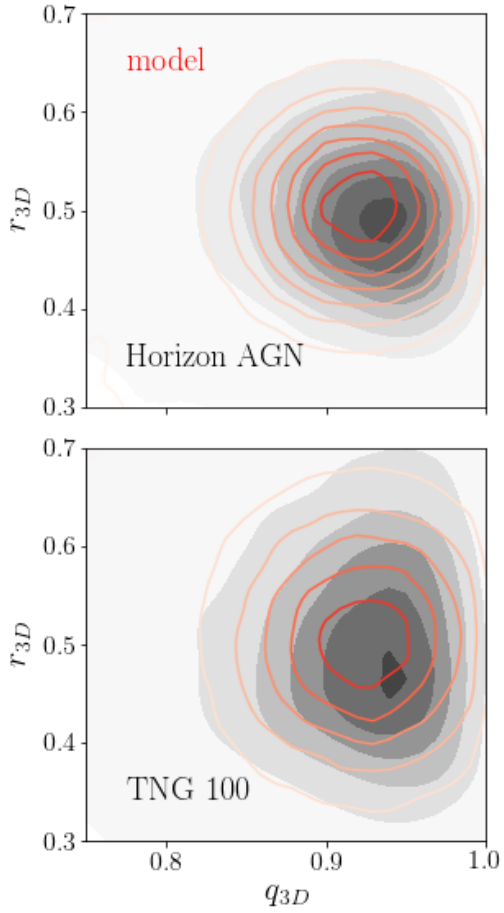

Figure A1. Distributions of the axes ratios $q_{3D} \equiv C_{3D}/A_{3D}$ and $r_{3D} \equiv C_{3D}/A_{3D}$ of disk galaxies in the HAGN and TNG100 simulations at $z = 1.0$. These distributions are compared to the $P(q_{3D}, r_{3D})$ model from equation (5), which was fitted to the marginalized distributions of q_{3D} and r_{3D} as shown in Fig. 12.

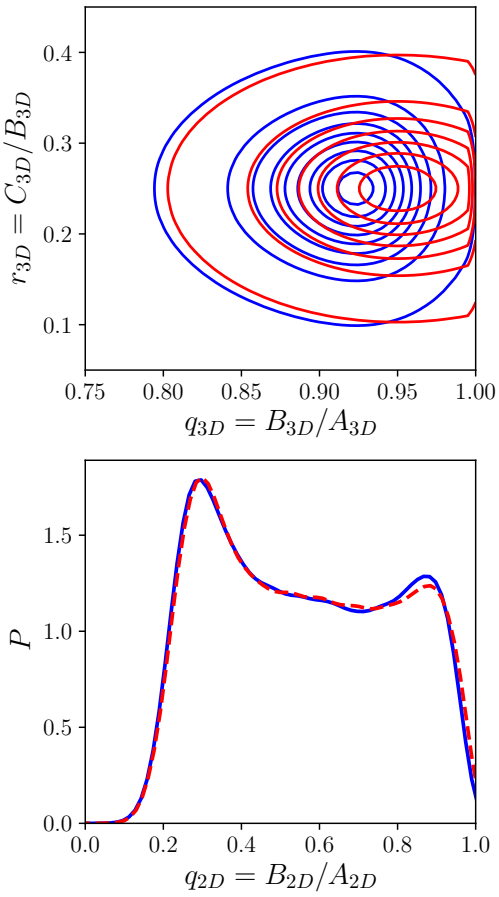

Figure A2. *Top*:model for 3D axes ratio distribution with and without skewness in the q_{3D} dimension (blue and red contours respectively). *Bottom*: Corresponding predictions for the 2D axes ratios distribution. The skewness as a very small affect on the 2D axis ratios.

results mainly from the absorption of light in the blue part of the spectra. This resulting dimming of the observed light can be seen in the central panels of Fig. B1: the apparent i-band magnitudes increase as q_{2D} decreases. In contrast to the color index, the correlation between between apparent magnitude and 2D axes ratios is tighter at higher redshift. This might result from the fact that the i-band filter corresponds to smaller rest-frame wavelengths at higher redshift, which leads to a stronger absorption. In the same panels we see that dust extinction can shift the apparent magnitudes below the detection limit. This effect can bias the q_{2D} distribution towards rounder face-on objects, in particular at high redshift. The effect is amplified when the magnitude limit of the sample is decreased. As a consequence, the inclinations of the remaining galaxies are biased towards face-on orientations. In order to mitigate these biases we select objects with absolute i-band magnitudes below -21.5, which appear not to be affected by the apparent magnitude cut of $m_i < 24$ for $z < 1.0$, used for selecting our volume limited sample.

APPENDIX C: DEPENDENCE OF GALAXY SHAPES ON COLOR

The galaxy shape measurements used in this work are based on ACS imaging in the F814W filter. This filter corresponds to a different rest-frame wavelengths at each source redshift. which can affect the observed shape of a given galaxy if its color is not uniformly distributed (for instance, due to extinction and reddening by dust or patchy star formation). We study this effect on the distribution of apparent axes ratio, measured in synthetic images of disk galaxies from the TNG100 simulations at $z = 0.0$, produced by (Rodriguez-Gomez et al. 2019) (see Section 2.2.3). The shapes are measured on images in the SDSS i- and g-bands, which correspond roughly to the ACS F814 band at $z = 0.0$ and $0.5 < z < 1.0$ respectively, as illustrated in Fig. C2. We find that the change of the apparent axes ratio distribution is weak, compared the the shot-noise errors, which we expect for our COSMOS samples (see Fig. 15). This result lines up with findings from Georgiou et al. (2019), who report a minor difference between galaxy ellipticities measured in different filters of the KiDS survey. Ryden (2006) show that axes ratios measured in the K_s and B band are strongly scattered, but not biased.

This paper has been typeset from a TEX/LATEX file prepared by the author.

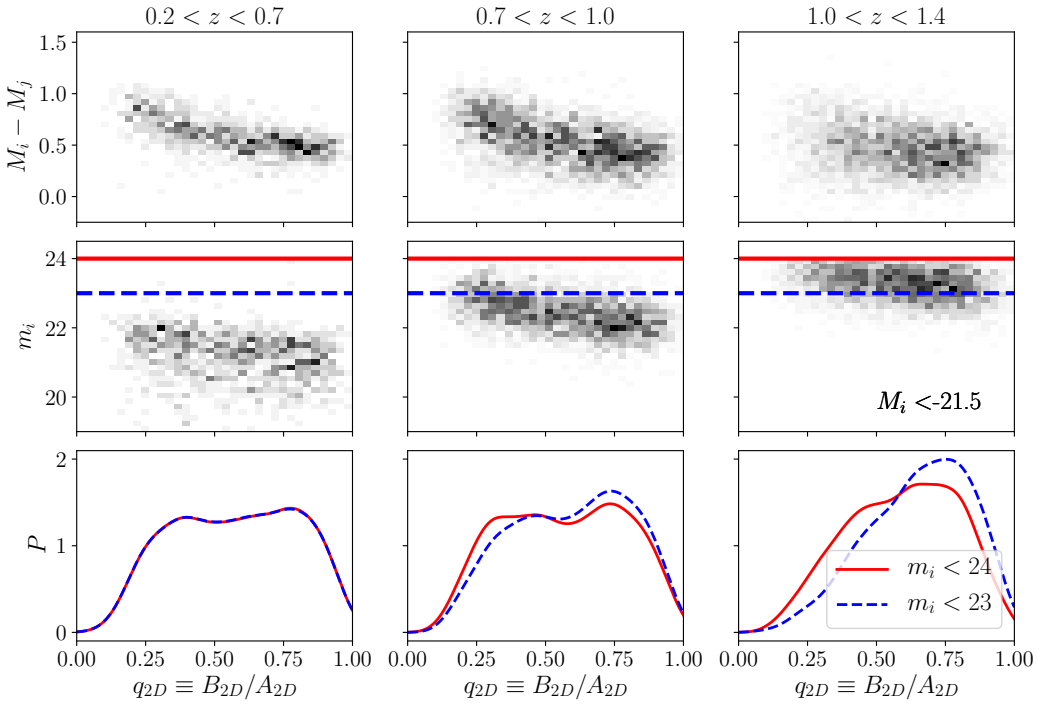

Figure B1. Apparent 2D axes ratios q_{2D} of disk dominated galaxies in COSMOS with absolute i magnitudes brighter than $M_i = -21.5$ versus the rest-frame color index and the apparent i band magnitude (top and bottom panels respectively). The solid red line in the central panel indicate the apparent magnitude cut of our volume limited sample. The dashed blue line illustrates how a decrease in the apparent magnitude cut can bias the q_{2D} distribution, shown in the bottom panels.

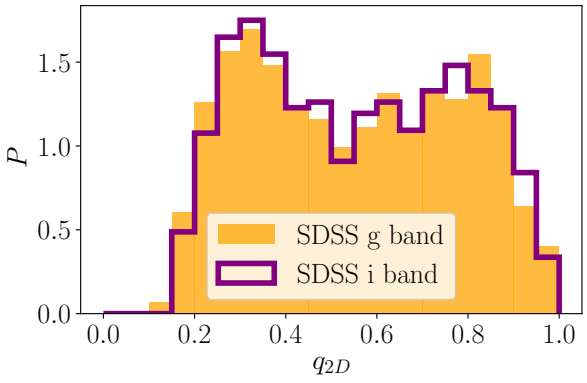

Figure C1. Distribution of apparent 2D axes ratios, measured from synthetic images of disk galaxies in the Illustris TNG100 simulation at $z = 0.0$ in the SDSS g- and i-bands.

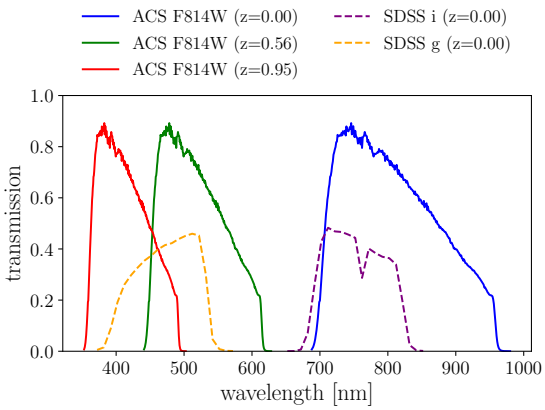

Figure C2. Filters of the SDSS g- and i-bands and to the ACS F814W filter used for the imaging in the COSMOS survey (dashed and solid lines respectively). F814W filter covers the near infrared wavelengths at $z = 0.0$, which corresponds to red and green wavelengths at the lowest and highest redshift bin used in our analysis (with mean redshifts of $z = 0.56$ and $z = 95$ respectively).